<center>ABSTRACT</center>

<center>CROSS VALIDATION OF OBSERVATIONS FROM THE GPM DUAL-FREQUENCY

PRECIPITATION RADAR AND DUAL-POLARIZATION S-BAND GROUND RADARS</center>

This research presents a comparative study of observations and various products of the Global Precipitation Measurement (GPM) Mission Satellite with dual polarization S-Band Ground Radars. The GPM mission is a joint venture by the NASA and the JAXA. The radar on board the core observatory is a dual-frequency precipitation radar (DPR) capable of simultaneously operating at 13.6 GHz (Ku band) and 35.5 GHz (Ka band). The DPR is expected to revolutionize the way precipitation is measured from space through its dual-frequency observations. Ground Validation is one of the most critical aspects of the GPM mission. The best way of doing this is by direct comparison of the space-based observations with well calibrated dual polarization ground radar measurements. Before any direct comparisons can be made, volume matching of the data is necessary due to the difference in observation geometry and resolution volume of both the system. In this study, a methodology developed by Bolen and Chandrasekar (2001) for aligning TRMM satellite data with ground radar data is followed. This technique was extended by Schwaller and Morris (2011). Radar reflectivity and rainfall rate product comparison study have been performed in detail. Vertical profiles have been studied thoroughly. Various case studies of simultaneous GPM-DPR and ground radar observations have been carefully chosen. Ground validation operational NEXRAD sites have been considered from all over the USA. Comparison studies with research radars such as CSU-CHILL and NASA N-POL have also been conducted. The GPM satellite's profile classification module's products are also evaluated. Results from Hydrometeor classification method by Bechini and Chandrasekar (2015) for ground radars have

been extensively used for validating DPR's melting layer detection capability in different types of precipitation system. In this study, a new method developed by Le et al (2017) for identification of snow falling on the ground has been considered. Ground validation comparisons have been performed with observations from ground radars and the results are presented.

TABLE OF CONTENTS

CHAPTER 1

INTRODUCTION

1.1. MOTIVATION AND BACKGROUND

The first space borne weather radar was carried by the Tropical Rainfall Measurement Mission (TRMM) satellite. Launched in November, 1997 as a joint mission by the NASA (National Aeronautics and Space Administration) and the JAXA (Japan Aerospace Exploration Agency), the TRMM satellite's scientific objective was to provide a quantitative precipitation map over the tropical and sub-tropical regions of Earth for better understanding the hydrological cycle [3]. After a successful span of 17 years, the TRMM came to an end on July 2015. The Global Precipitation Measurement (GPM) mission was launched to provide next generation observations of precipitation from space. The core satellite was launched in February 2014 by the JAXA. It is expected to improve the precipitation mapping from space by covering a wider range of latitudes i.e. from 65° N to 65° S.

The planning for GPM mission started very early and new algorithms for the dual-frequency radar were on development [4]. Precipitation observations from space at Ka band was never done before. Study of electromagnetic wave propagation at this high frequency and it's effects on the retrieval algorithms were very crucial for system performance and development. One of the fundamental obstacle that needed to be overcome was the unavailability of Ka band data from space. Thus, before launch, retrieval algorithms based on Ka-band observations were tested and validated on synthetic data. Various research have been focused on simulating data at Ka band from the TRMM-PR's Ku band measurements. Evaluation of algorithm performance on synthetic data can be found in the studies conducted by Direk

Khajonrat [5] [6]. The evaluation presented showed promising results. A second generation airborne precipitation radar (APR-2) was developed by NASA Jet Propulsion Laboratory (JPL) with the same frequency channels as the GPM-DPR for validation purposes. Though the vertical range resolution of the GPM-DPR and APR-2 didn't match, APR-2 radar data helped in GPM-DPR validation studies [7].

After launch, the availability of GPM-DPR Ku-band and Ka-band observation data facilitated ground validation studies. Since previous studies were mostly based on simulated data, validation needed to be done on post launch data. Simultaneous dual-polarization data collected from radar located all over the USA are used to comparison study. Previously, several validation studies has been conducted for the TRMM-PR [8] [9]. These have been carefully studied and similar procedures are followed for the GPM-DPR in this work. One of the major difficulty in this kind of comparison is the difference in viewing geometry of the space-based and ground-based system. To this end, in 2001 Bolen and Chandrasekar [10] proposed a methodology for aligning space-based and ground-based radar. A similar procedure has been followed and used in this work for the GPM-DPR. Volume matching technique has also been implemented and used. In sum, the comparison results of the GPM-DPR and ground radar would provide a theoretical basis for the evaluation of the DPR algorithms.

1.2. Objectives

The main objective of this research is to cross validate different measurements and products of GPM-DPR satellite with ground radars which in turn would help in evaluation of the performance of various algorithms presently used by the GPM satellite for microphysical

retrievals. The main focus of this work is the comparison of radar reflectivity factor since it is the fundamental product used in precipitation estimation. Other products from profile classification module which helps in precipitation retrieval are also validated. The ultimate goal is to understand, quantify and resolve errors and biases in GPM satellite measurements and precipitation retrievals at large scale. The objectives of this validation study can be enumerated as follows.

(1) To compare the radar reflectivity factor and rainfall rate.

(2) To evaluate the products of the current DPR profile classification module.

(3) To further refine GPM-DPR algorithms.

1.3. Overview of this Thesis

This document is organized as follows. In Chapter 2, a background on GPM mission is presented along with a brief overview of the working principles of dual-frequency precipitation radar. An introduction to dual-polarization radar has also been provided. Next, in Chapter 3, the importance of ground validation in GPM satellite's retrieval algorithm development and evaluation is discussed. The primary focus of this chapter is the volume matching procedure between space and ground radar. Technical specification of different ground validation radars used in this study are also described. In Chapter 4 detailed quantitative comparisons between the reflectivity measured by both GPM-DPR and ground radar are presented. Space borne radar rainfall rate and ground radar products are also compared qualitatively for selected case studies. Statistical scores are used for evaluation purposes. Time series of GR-DPR bias in reflectivity factor is also studied for four well calibrated ground radars. In Chapter5 validation studies of products from the GPM profile classification module has been performed. A very brief description of the GPM profile classification

algorithm is presented. Hydrometeor classification results from ground validation radars are compared with GPM products such as melting layer height and surface snowfall flag. At the end, in Chapter 6, a summary of this research work is presented. Finally, scope for improvements are discussed and suggestion for future work is stated.

CHAPTER 2

Background on Spaceborne Radars

2.1. Introduction

Measurement of quantitative precipitation globally remains one of core aspect of studying Earth's atmosphere. The variation of the Earth's water cycle is recognized as one of the most important factors contributing to global climate change. Before the time of space-borne radars meteorologists and scientists only relied on ground based instruments for sensing of Earth's atmosphere. After the advent of dual polarization capability, the role played by ground radars became more important in studying the relation of drop-size distribution and rainfall rate and also the microphysics behind hydrometeor formation [11]. But it was not an exhaustive process since the radar's observational range is limited and as a result most of the oceans remained unobserved. Something was needed which could remotely sense Earth's atmosphere over the oceans and provide high resolution data almost in real-time manner. This was made possible by the Tropical Rainfall Measurement Mission (TRMM), launched in 1997 [12]. The precipitation radar carried by TRMM satellite(TRMM-PR) became the first spaceborne weather radar to measure precipitation over the tropics. Launched with a life expectancy of 3 years and 2 months only, TRMM continued for an unexpected successful 17 years and was finally taken down on June 16̂th, 2015. Data acquired by the TRMM brought about new insights of precipitation in tropical region where 70 % of Earth's rainfall occur annually. Various findings have contributed to explicating Earth's water cycle and global climate change. These precious information not only helped in better weather forecasting but also drought monitoring and storm/flood warnings. Like any other satellite TRMM had a finite lifetime and thus it was very important to plan the next follow-on mission from

early. GPM's planing started well in advance from 2002 [13] when TRMM was in orbit. The accomplishments and heritage of TRMM was carried on by the GPM mission. TRMM had already revolutionized the way of observation of Earth's atmosphere and GPM was poised to further enhance this by its ability to independently measure at two frequency channels (Ku and Ka band).

2.2. The GPM Mission

The Global Precipitation Measurement (GPM) earth observing mission is a joint collaboration by the National Aeronautical and Space Administration (NASA) of USA and Japan Aerospace Exploration Agency (JAXA). Many additional partners from world wide supported this mission. Among them are the Indian Space Research Organization (ISRO), Centre National dtudes Spatiales (CNES), the European Organization for the Exploitation of Meteorological Satellites (EUMETSAT), the National Oceanic and Atmospheric Administration (NOAA). The core satellite shown in 2.1 was launched on 27th February, 2014 from Tanegashima Space Center, Japan.

Unlike TRMM, which only observed the tropical region, the GPM's observation limits has been escalated to cover a greater extend of Earth. Flying over the Arctic Circle 65ô N to the Antarctic Circle 65ô S would enable GPM to observe higher latitudes where winter precipitation is mainly dominated over rainfall. This is a huge achievement for GPM since TRMM with its single frequency capability was not able to measure accurately light rain (10 mm/hr or less) and snow. Observations through two independent frequency band at 3.6 GHz (Ku band) and 35.5 GHz (Ka band) makes this possible. The GPM Microwave Imager (GMI) also is a multi-channel instrument with frequency channels ranging from 10

FIGURE 2.1. Photograph of GPM satellite launch from Tanegashima Space Center, Japan at 1:37 p.m. EST, Feb 27, 2014. Image source: http://www.nasa.gov/mission˙pages/GPM/launch

GHz to 183 GHz. Both the DPR and GMI work simultaneously to cross calibrate each other and they serve as a reference standard for the other satellites in constellation. Thus the measurements from the DPR-GMI coupled with those from polar orbiting satellite in its constellation would provide a global picture of precipitation in a near real time manner for every 3 hours.

The main goals of the GPM Mission can be summarized as follows:

- Improving weather forecasting
- Better understanding Earth's water cycle variability and climate change

- Calculating better rainfall rate estimate by providing accurate particle size distribution from a wide spectral range.

- Improving winter precipitation measurement such as light rain and snow over higher latitudes.

(A) GPM Core Observatory
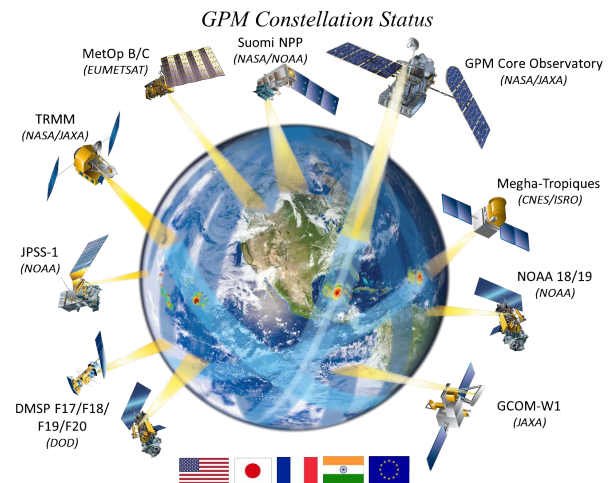
(B) GPM Constellation

Figure 2.2. Illustration of multiple GPM constellation satellites and Core Observatory. Image source: http://pmm.nasa.gov/multimedia/images/GPM

2.2.1. GPM Dual-frequency Precipitation Radar (DPR). The heart of the GPM satellite is the Dual-frequency Precipitation Radar (DPR) along with the GPM Microwave Imager (GMI). The improved combined radar-radiometer observations will allow to study cloud microphysics more profoundly. The GPM-DPR is the second of its kind space borne weather radar after TRMM-PR. The DPR consists of Ku-band (13.6 GHz) and Ka-band (35.5 GHz) channels. It provides high resolution three dimensional precipitation data over land and ocean which would enable to study the vertical structure of storms.

One of the main reasons for adding the Ka band channel is to improve the rainfall rate estimation over TRMM's rainfall product. A major source of error crops into the conversion

of reflectivity to rainrate due to varying rain drop size distribution over region to region. Since the hydrometeors falls in Mie scattering region for Ka band, accurate information can be extracted for particle size distribution which in turn helps in estimating rainrate. The Ka band would also detect accurate melting layer height even in convective precipitations. This information is even needed by the passive radiometer for rainfall estimate. Lastly, winter precipitations such as snow and light rain also falls under the Mie scattering region for Ka band thereby increasing the sensitivity of the satellite. All this is made possible by the new Ku - Ka band combined dual-frequency algorithm. The figure 2.3 depicts a cartoon of DPR's observation of vertical reflectivity profile. Rainfall rate estimation, melting layer detection and precipitation type classification depends on the retrieved drop size distribution for which the study of vertical profile is very important.
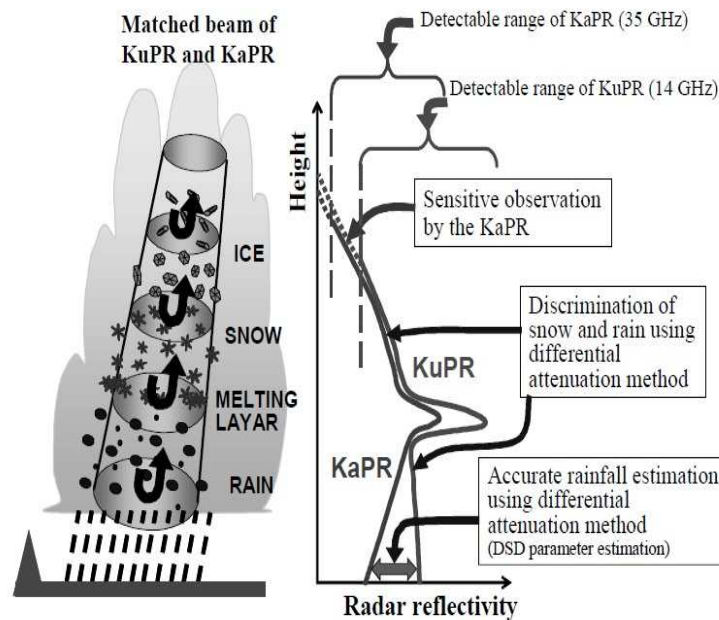
FIGURE 2.3. Concept of DPR dual-frequnecy observation. Image source: Senbokuya et al. [1]

Each radar in DPR consists of active phased array elements (128 slot array antennas) capable of 49 simultaneous beam formations. A detail design specifications can be found in the work of Senbokuya et al [1]. The antenna and the pulse repetition time is designed such that the DPR can observe at least 19 Km from the sea level. There are three type of scan performed by the DPR. Figure 2.4 shows the scan strategy.
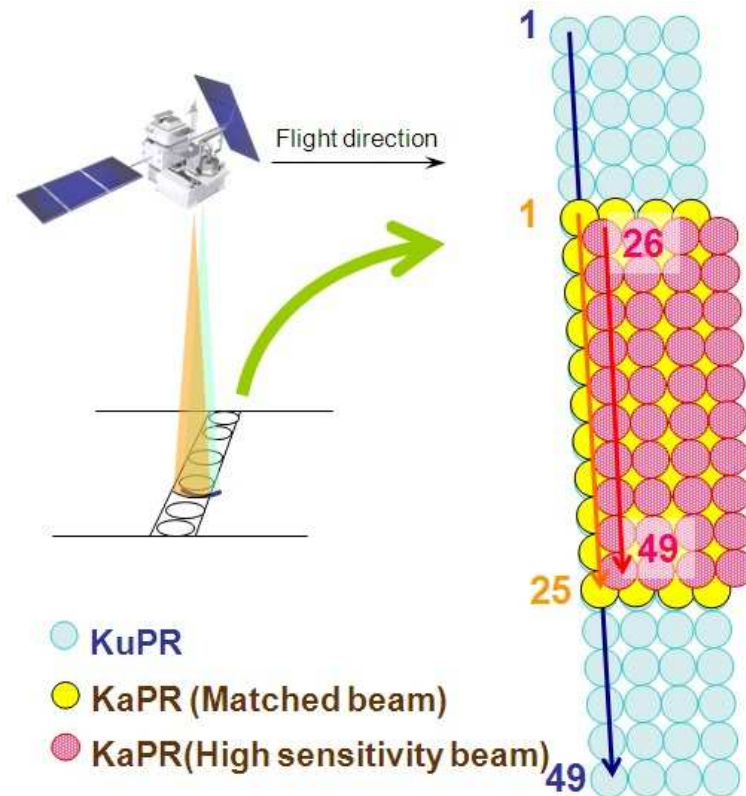
FIGURE 2.4. GPM-DPR scan strategy. Image taken from GPM Level 2 algorithm theoritical basis document

The first type of scan is called the normal scan which resembles that of the TRMM Ku channel. Here the radar scans with only the Ku band with all the 49 beams. Each footprint has a diameter of approximately 5 km which gives a scan swath of 245 Km. The range resolution of this mode is 250 m. The second type of scan is done by the Ka band channel

where the beams are matched with the central 25 beams of the Ku band channel providing a total swath of 120 Km. This scan is called the mixed scan. The last type of scan is called the high sensitivity scan where all the 49 beams of Ka band are used but are interlaced with the middle 25 beams of Ku-band. Range resolution for this mode is 500 m. Since the radar echoes are over sampled at twice the rate, the final resolution that we get is 125 m for normal and mixed scan and 250 m for high sensitivity scan. The narrow bandwidth of the KaPR can be accounted for sidelobe clutter contamination for large scan angles. The table 2.1 summarizes GPM-DPR design specifications.

2.2.2. Theoretical basis of DPR algorithms

. It is predicted that dual frequency data as opposed to TRMM PR's single frequency data will provide more accurate information on the particle size distribution from non-Rayleigh scattering effects which in turn would help in better estimating the melting layer height even in strong convective precipitation. Unlike TRMM's single frequency (Ku band) algorithm [14], the DPR's algorithm depends on the use of dual frequency data often called measured dual frequency ratio or $DFRm$. Basically the radar observes targets by the back scattered power it receives from transmitting short electromagnetic pulses. This returned power is known as radar echo. In case of a weather radar the objects of interest are precipitation material such as rain drops, snow flakes, hails, clouds and different hydrometeor. In general the received power $P(r)$ which is a function of range is proportional to the radar measured reflectivity factor $Z_m(r)$.

(1)
$$P(r) = \frac{C\,|K|^2}{r^2} Z_m(r), \qquad where \quad K = \frac{m^2 - 1}{m^2 + 2}$$

TABLE 2.1. GPM-DPR Specifications from GPM Level-2 Algorithm Theoritical Basis Document

Item	KuPR	KaPR
Swath Width	245 Km	120 km
Range Resolution	250 m	250/500 m
Spatial Resolution	5.2 Km at Nadir	5.2 Km at Nadir
Beam Width	0.71ô center beam	0.71ô center beam
Transmitter	128 Solid State Amplifiers	128 Solid State Amplifiers
Peak Transmit Power	1012.0 Watts	146.5 Watts
Pulse Repetition Freq	4000 to 4500 Hz	4000 to 4500 Hz
Pulse Width	two 1.6 μ s pulses	two 1.6 μ s pulses in matched beams two 3.2 μ s pulses in interlaced scans
Beam Number	49	49 (25 in matched beams and 24 in interlaced scans)
Min measurable rain rate	0.5 mm/h	0.2 mm/h
Beam matching error	Under 1000 m	Under 1000 m
Observable range	19km to Surface (to -5 km near nadir)	19km to Surface (to -5 km near nadir)
Dynamic range	From -5dB below the system noise level to +5dB above the nominal maximum surface echo level	From -5dB below the system noise level to +5dB above the nominal maximum surface echo level
Receiver power accuracy	+/- 1dB	+/- 1dB
Scan Angle	+/-17ô Cross Track	+/-17ô Cross Track
Frequency	13.597 and 13.603 GHz	35.547 and 35.553 GHz
Bandwidth	14 MHz	14 MHz
Max. Mass	472 Kg	336 Kg
Max. Power	446 W	344 W
Science Data Rate	109 kbps (The total of KuPR and KaPR is 190 kbps)	81 kbps (The total of KuPR and KaPR is 190 kbps)
Housekeeping Data Rate	1 kbps	1 kbps

C is the radar constant and K is defined as a function of refractive index m of the scattering particles. The radar constant takes into account of all the electrical specifications of radar such as antenna beamwidth, antenna gain, wavelength of pulse, transmission power, pulse repetition frequency etc. Given range and radar constant, the radar reflectivity factor Z_m can be calculated by the equation 1. Of course it depends on the distribution of the

precipitation particles in the volume defined by the antenna beam and pulse width. When electromagnetic waves travel through precipitation medium it suffers attenuation which is not accounted on the equation 1. Thus the attenuation corrected effective reflectivity factor Z_e can be defined as

(2) $$Z_e(r) = A(r)Z_m(r),$$

where $A(r)$ is the two way attenuation of the wave at distance r. Effective reflectivity Z_e again can be expressed in terms of the pulse wavelength λ, radar cross section $\sigma_b(D)$ of particles with diameter D and density $N(D)$ as

(3) $$Z_e = \frac{\lambda^4}{\pi^5 |K|^2} \int \sigma_b(D)N(D)dD$$

Rainfall rate can also be expressed in terms of drop size distribution $N(D)$, fall velocity $v(D)$ and volume $V(D)$ of the scattered particles as

(4) $$R = \int V(D)v(D)N(D)dD$$

Single frequency radar such as TRMM-PR is only able to retrieve one parameter of the rain drop size distribution. For example let D^* be that parameter. It can be either the median drop diameter or the total number of drops at each range bin of the vertical

profile. In this case Z_e only would depend on one parameter of the distribution function i.e. D^*. Since rainfall rate would also depend on single parameter, once Z_e is measured we can get the distribution $N(D)$ specified by D^* corresponding to Z_e and from that rainrate R. However, in nature drop size distribution varies from place to place, from season to season and with type pf precipitation. It is not sufficient to characterize this variation with only a single parameter which is a major source of error for single frequency rainfall rate estimation. This can be overcome by modeling DSDs with two parameter. Let N^* and D^* be the two parameters for $N(D)$. Z_e would now depend on both of these parameters. To solve two unknowns we need two independent equations. DPR with its dual frequency capability observes precipitation at two frequency independently in which Ka band observations falls under non-Rayleigh scattering.

(5) $$Z_e\_Ku(N^*, D^*) = \frac{\lambda^4}{\pi^5 \, |K|^2} \int \sigma_{bku}(D) N(D; N^*, D^*) dD$$

(6) $$Z_e\_Ka(N^*, D^*) = \frac{\lambda^4}{\pi^5 \, |K|^2} \int \sigma_{bka}(D) N(D; N^*, D^*) dD$$

Thus we have equations 5 and 6 for Z_e at Ku band and Ka band respectively which can used to solve N^* and D^*. This is turn would end up in better rainfall rate estimation. It is the basis of rainfall rate observation from dual frequency radar. The measured reflectivities should be first attenuation corrected to arive at the effective reflectivities.

If the Ku band measured reflectivity is taken as $Z_m(K_u)$ and the Ka band measured reflectivity is taken as $Z_m(K_a)$, then the $DRFm$ is defined as the difference of the two reflectivities. (We take the difference since both are in logarithmic scale). The shape of the $DFRm$ vertical profile is both controlled by the physics of scattering and the rate of differential attenuation at the two frequency.

$$(7) \qquad\qquad DFRm = Z_m(K_u) - Z_m(K_a)$$

2.2.3. Brief structure of DPR algorithms

. After the processing of raw observed data, various products are generated. This is categorized into different modules. Each module has its own algorithm structure. Level 2 GPM-DPR algorithms are primarily focused with generating products derived from radar observations only. Radiometric observations from the Microwave Imager are not considered here. The main purpose of the modules is to interact among each other to get a general characteristic and type of precipitation, attenuation correction, estimation of rainfall rate and phase transition height in various precipitation system whenever dual frequency data are available.

Both single frequency (Ku only algorithm & Ka only algorithm) and dual frequency algorithm are deployed on the DPR. The latter takes the input from both single frequency algorithms. The Ku only algorithm is executed for both inner and outer swaths while the Ka only algorithm is only executed for the inner swath of mixed and interleaved scans. The dual frequency algorithm is used for the inner swath only for all the three scans.
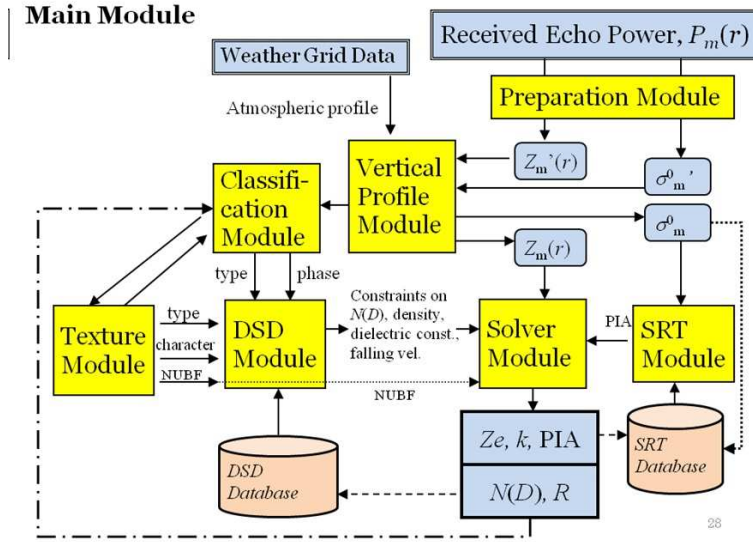
FIGURE 2.5. Picture of different DPR algorithm modules. Image taken from GPM Level 2 algorithm theoritical basis document

The image 2.5 depicts the underlying framework of all the algorithms. The main module is entrusted with managing the whole procedures while employing several sub modules. First the received raw power is converted to measured reflectivity in the preparation module. In the Vertical Profile module the reflectivity is corrected for attenuation from non precipitating particles such as cloud liquid water, atmospheric water vapor, molecular oxygen etc. The main process of obtaining the DSD parameters is carried out in the Solver module along with determining specific attenuation and path integrated attenuation. The solver module takes input from all the other modules such the SRT module and DSD module. The DSD module is responsible for maintaining the terms of the in the DSD equations such as α, β, $N(D, D^*)$, fall velocity and dielectric constant based on the precipitation characteristics determined by the Classification Module. This module is responsible for classifying different types of precipitation and for detecting the melting layer height. This will be addressed in detail in chapter 5.

CHAPTER 3

Ground Validation of GPM-DPR with S-Band Ground Radars

3.1. Introduction to Ground Validation

Ground Validation of GPM satellite observation is one of the most critical aspect of the mission. After its launch in year 2014, various grounds validation studies have been conducted using an extended GPM ground Validation Network (VN) [2]. The validation network consists of several ground based radars operated by National Oceanic and Atmospheric Administration (NOAA) and Department of Defense (DoD) throughout the continental USA. These radars, operated at the S-Band, are technically called by the name of Weather Surveillance Radar 1988 Doppler or WSR-88D. They are popularly known as Next Generation Weather Radar (NEXRAD) [15]. An initial validation network developed for the TRMM precipitation radar contained 21 NEXRAD sites which falls within the satellite's view. A detail description can be found in [16].Since GPM has a larger latitude coverage i.e. from 65^oN to 65^oS, the already existing network was extended to accommodate new NEXRAD sites. A picture depicting the GPM validation network is shown below. The circles indicate 100 Km range radius of ground radars.

Other than the NEXRADs, research radars such as CSU-CHILL and NASA N-POL radars are also considered for ground validation purposes. Being research radars, both of them performs range height indicator or RHI scan which can be particularly useful in validating vertical profiles from DPR observations for its higher resolution in the vertical direction. This is an unique advantage over the plan position indicator or PPI scanning
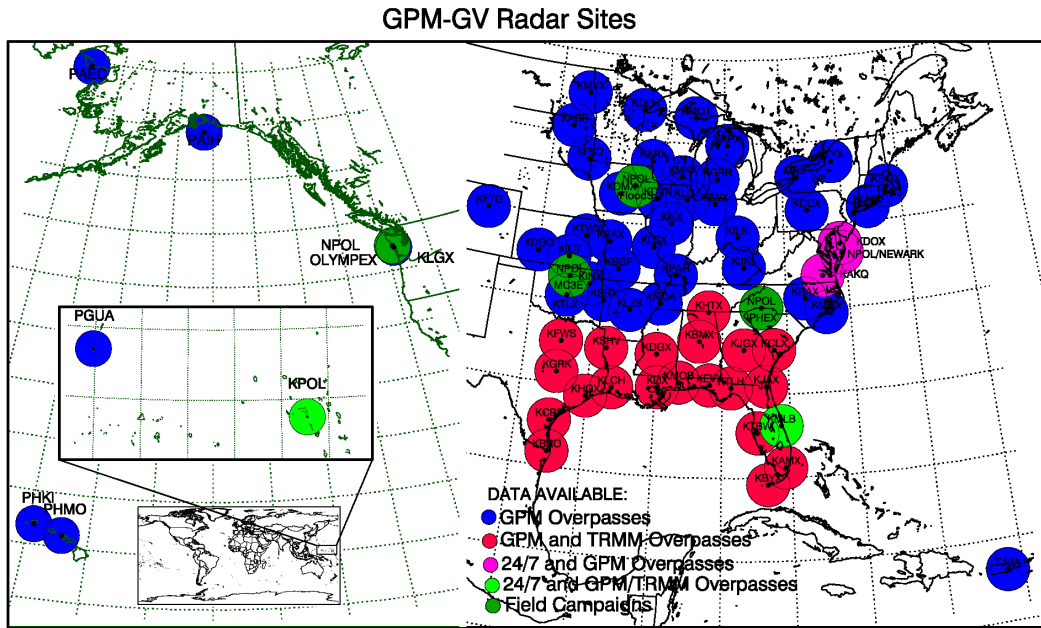
FIGURE 3.1. GPM GV Radar Sites. Sites marked in blue is covered by GPM overpasses only. Circles marked in red are the initial sites for TRMM validation network. They also fall under the GPM network. Circles marked in pink are those 3 sites which are monitored 24 hrs. Lastly, circles marked in green shows the sites for various field campaigns conducted by NASA. Image taken from https://gpm-gv.gsfc.nasa.gov

NEXRADs. In this study, 7 different NEXRAD sites along with CSU-CHILL and NASA N-POL radar are chosen for validation study. Ground validation is a necessity to identify and resolve significant differences between satellite observations of radar reflectivity and rainfall rate, and similar observations from ground radar. The ultimate goal of this study is to further improve and refine the algorithms presently used in DPR for various microphysical retrievals.

3.2. INTRODUCTION TO DUAL-POLARIZATION GROUND RADARS

One of the most prominent instruments for remote sensing are weather radars. They are used for detection of severe weather, flood warnings, weather forecasts and precipitation estimation. It is based on the principle of scattering of electromagnetic energy by particles.

The radar transmits a series of electromagnetic pulses and receives the back scattered energy from targets. This scattered energy is measured in terms of power and voltage by the radar. The measured power is then digitally sampled and the data is further processed by various algorithms in order to make sense. A detailed theory on the working principles of weather radars is given in the book by Bringi & Chandrasekar [17]. Targets can be anything which scatters electromagnetic waves.

Recent advancement enables the radar in transmitting and receiving of electromagnetic energy in two type of polarization. The type of polarization can be determined by the direction of the variation of the electric field vector in 3-dimensional space with respect to the propagation of the electromagnetic wave. Polarization can be of several types namely horizontal, vertical, slant, elliptical and circular of which the most common polarization used in weather radar are horizontal and vertical. All weather radars in the continental USA are have been upgraded to dual polarization. Dual-polarization has a significant advantage over single polarization in retrieving particle shape and sizes. The fundamental quantities measured by a radar is power and velocity. Other parameters are derived from it. These observables can be expressed in terms of drop size distribution (DSD).

3.2.1. DROP SIZE DISTRIBUTION. In the field of remote sensing and meteorology, the targets of interest are different types of hydrometeors. They can be rain, hail, snow, graupel, ice crystals, dendrites, so on and so forth. These hydrometeors are result of precipitation by the clouds in atmosphere and they vary in shape and size. Understanding particle size distribution along with scattering microphysics are of fundamental importance in determining characteristics of precipitation and it's estimation. The natural variability in drop size

distribution (DSD) of rain can be sufficiently described by a gamma distribution. This has been shown by Ulbrich in 1983 [18]. Testud showed that the gamma DSD model can be expressed in a normalized form which is

$$(8) \qquad N(D) = N_w f(\mu) \left(\frac{D}{D_o}\right)^{\mu} e^{-\Lambda D}$$

where

$$(9a) \qquad \Lambda = \frac{3.67 + \mu}{D_o}$$

$$(9b) \qquad f(\mu) = \frac{6}{3.67^4} \frac{(3.67 + \mu)^{\mu+4}}{\Gamma(\mu + 4)}$$

$N(D)$ $(mm^{-3}m^{-1})$ is the number of drops per unit volume per unit diameter of size interval D (mm) and D+Δ D(mm), N_w $(mm^{-3}m^{-1})$ is called the normalized intercept parameter of an equivalent exponential DSD which has the same water content as the gamma DSD. μ is the shape parameter, and Λ (mm^{-1}) is the slope parameter. D_o (mm) is the median volume diameter in (mm) which is defined such that drops up to size D_o contribute to half the rainwater content. Γ () represents gamma function. Thus μ, D_o, and N_w are the 3 most important parameter of the drop size distribution which controls the shape of the curve.

3.3. Radar Moment Calculation

The most fundamental parameter, radar reflectivity, can be derived from a given drop size distribution. Other parameters namely differential reflectivity and specific differential

phase can also be expressed as different moments of the gamma distribution. Reflectivity at the horizontal polarization denoted by Z_h can be calculated as

(10)
$$Z_h = \frac{\lambda^4}{\pi^5 |K_w|^2} \int_D |S_{hh}(r,D)|^2 N(D) dD$$

Here, $Shh(r,D)$ is the back scattering cross section at horizontal polarization, K_w is the dielectric constant of water, λ is the radar wavelength, d is the drop diameter and r is the distance of the drop with respect to radar. The reflectivity is also known as the water equivalent reflectivity factor since in the calculation, dieletric constant of water is used as apriori information of the target hydrometeor is not known. In the Rayleigh scattering regime, the back scattered cross section is proportional to D^6. The equation 10 can be simplified to

(11)
$$Z = \int_D N(D) D^6 dD$$

Thus the reflectivity factor can be approximated as the $6^t h$ moment of the DSD. This is also known as the Rayleigh approximation. Generally S-Band radars operates at 2.7 GHz which falls under this regime. It should be noted that at higher frequencies the scattering regime falls in non-Rayleigh or Mie region where this approximation is not valid. The differential reflectivity is denoted by Z_{dr} is calculated as

$$(12) \qquad Z_{dr} = \frac{\int_D |S_{hh}(r, D)|^2 N(D) dD}{\int_D |S_{vv}(r, D)|^2 N(D) dD}$$

It can be noticed that Differential reflectivity is independent on the number of drops but depends directly upon the drop axis ratio. Another measured parameter is called the differential phase and is denoted by Φ_{dp}. As the pulse propagates through medium, the cumulative change in phase between horizontal and vertical polarization is given by Φ_{dp}. The radar cannot directly measure differential phase. It rather measures Ψ_{dp} which not only considers the forward propagation phase change but also the back scatter differential phase δ_{co}.

$$(13) \qquad \Psi_{dp}(r) = \Phi_{dp}(r) + \delta_{co}(r)$$

Differential Phase (Φ_{dp}) can also be expressed as the range derivative of Specific Differential Phase denoted by K_{dp}.

$$(14) \qquad \Phi_{dp}(r) = \int_0^r K_{dp}(r) dr + \delta_{sys}$$

Here δ_{sys} is a constant term which denotes built in system phase. This is usually an adjustable parameter and often considered as 0 in calculations.

$$(15) \qquad K_{dp} = \frac{2\pi}{k_0} \operatorname{Re} \int_D N(D) \left[\hat{h} \cdot \vec{f}(r, D) - \hat{v} \cdot \vec{f}(r, D) \right] dD$$

The specific differential phase can be expressed in terms of forward scattering amplitude at both polarization.

3.4. Different S-Band Ground Radars used for validation

3.4.1. Weather Surveillance Radar (WSR-88D). The Weather Surveillance Radar are operational weather radars operated by National Oceanic and Atmospheric Administration (NOAA) and Department of Defense (DoD). At present there is a deployment of 160 WSR-88D, also known as NEXRADs, throughout the continental USA. They operate 24x7 for supporting weather predictions and extreme weather warning. Recently, NEXRADs have been upgraded to dual-polarization. They operate at the frequency range of 2700 MHz to 3000 MHz. A typical NEXRAD system along with it's radome and support structure is shown in the figure 3.2 below.

The radar has a range resolution of 250m along the beam which is 1 degree wide. During normal operations the radar conducts a volume coverage pattern (VCP) in which it scans full 360 degree in azimuth and from 0.5 degree to 19.5 degree in elevation in steps of 14 PPI scans. There are different variety of VCP which are optimized for specific weather conditions and are deployed by the operational controls according to the observed meteorological event and desired data quality. Typical range of NEXRADs are till 400 Km. The table below summarizes typical specifications of a NEXRAD.

FIGURE 3.2. Picture showing a next generation weather surveillance radar system. The white round ball shaped encloser is the radome which is supported by mechanical structure. The radar is located within the radome. Image source: https://www.roc.noaa.gov/WSR88D/Engineering/NEXRADTechInfo.aspx

3.4.2. CSU-CHILL RADAR. The CSU-CHILL or Colorado State University - University of Chicago-Illinois State Water Survey Radar is a S-Band research radar located at Greeley, Colorado in USA. It is a dual polarization radar capable of transmitting a wide variety of polarization states. It was initially deployed in 1978 jointly by the University of Chicago and the Illinois State Water Survey. In 1990, the radar was transferred to Colorado and since then has been operated by CSU (Colorado State University). Key features of the radar is its ability to transmit and receive simultaneously at different polarization states, very sharp pencil beam antenna pattern, very high detection sensitivity and a very low integrated cross-polar ratio (ICPR2) antenna system. Recently, CSU-CHILL has been upgraded with a second transmitter at X-Band enabling it to transmit at dual frequency. A brief description of the CSU-CHILL National Radar Facility can be found in [?]. Being a research radar,

TABLE 3.1. Summary of the system specifications of NEXRADs

Transmitter	
Type	S-Band
Frequency	2700 MHz to 3000 MHz
Power at klystron output	700 KW peak
Average Power	300 to 1300 W
Pulse Width	1.57 and 4.71 μsecs
PRF short pulse	318 to 1304 Hz
PRF long pulse	318 to 452 Hz
Antenna	
Type	Parabolic dish (28 feet in diameter) with center feed horn
Polarization	Dual Pol (simultaneous horizontal and vertical transmit/receive)
Gain at 2850 MHz	45.5 dB (including radome loss)
Beamwidth at 2850 MHz	0.925 deg
First sidelobe	-29 dB
Radome	fiberglass foam sandwich frequency tuned, 39 foot truncated sphere
Radome two way loss	0.24 dB at 2850 MHz
Receiver	
Type	Coherent (stalo/coho)
Detection	digital IF with 16 bit analog to digital conversion of IF signal at 100 MHz
Digital Matched Filter BW	625 kHz, short pulse, 204 kHz, long pulse
Dynamic Range	93 dB minimum required
Intermediate Frequency	57.55 MHz
System noise figure	270K (2.7dB)
Receiver Noise	-114dBm (Short Pulse),-118dBm (Long Pulse)

CSU-CHILL is does both volume PPI scan and RHI scans. The range resolution is 150m along the beam. A picture of the CSU-CHILL radar is shown below in 3.3. A summary of technical specifications of the radar is also presented below in table 3.2.

3.4.3. NASA N-POL RADAR. The NASA N-POL radar is a S-Band mobile research radar operated by the NASA. Like the CSU-CHILL radar, it is also a dual-polarization radar.

FIGURE 3.3. Picture showing CSU-CHILL radar inside the radom encloser at the CSU-CHILL National Radar Facility. Image source: http://www.chill.colostate.edu/w/Facilities

It is capable of doing both PPI and RHI scans. Being a mobile radar, it is extensively used by the NASA for various GPM field campaigns. At times other than the field campaign, this radar is operated at the NASA's Wallops Flight Facility in Newark, MD, USA.

FIGURE 3.4. Picture showing NASA N-POL radar at the Wallops facility. Image Source: https://pmm.nasa.gov/science/ground-validation/npol

TABLE 3.2. Summary of the S-Band system specifications of CSU-CHILL Radar

Transmitter	
Type	S-Band
Wavelength	11.01 cm (2.725 GHz)
Peak Power	800 KW (per channel)
PRT Range	800 μs to 12000 μs
Polarization	Horizontal, Vertical, Alternating, Slant 45/135, Left/Right Circular
Waveform	Programmable, intra- and inter-pulse modulation supported
Antenna	
Shape	Parabolic dish (8.5m in diameter)
Feed Type	Scalar
Gain	43 dBi, including feed loss
Beamwidth	1.1^o
Maximum Sidelobe	-27 dB (in any ϕ plane)
Inter-channel Isolation	-45 dB (limited by ortho mode transducer)
ICPR	-34 dB (two-way)
Scan types	PPI (optional sector scan), RHI, fixed-pointing, vertically pointing
Max. slew rate	18°/sec
Receiver	
Sensitivity	-33 dBZ @ 1km (0dB SNR)
Noise Figure	3.4 dB
Noise Power	-113 dBm @ 1 MHz bandwidth
Dynamic Range	80 dB
Bandwidth	Programmable. Simultaneous 1 MHz and 5 MHz channels are available.
Range Resolution	Min: 30m, Typical: 150m programmable.
Max. Range Gates	6000
Clutter Suppression	Selectable Chebyshev/Elliptic notch filter.
Processing modes	Pulse Pair
Available data	Time-series (I/Q samples), polarimetric variables including KDP, available in real-time and archived data
Data Formats	Binary time-series files (with associated calibration info), Internal archive format, UF, netCDF, Nexrad Level II

TABLE 3.3. Summary of the S-Band system specifications of NASA N-POl Radar

Type	S-Band
Frequency	2.7 GHz to 2.9 GHz
Polarization	Horizontal, Vertical, Alternating
PRF	250 to 1200 Hz
Pulse Width	0.8 to 2 ms
Transmitter	850 KW Magnetron
Receiver	Vaisala RVP 900
Waveform	Programmable, intra- and inter-pulse modulation supported
Shape	Parabolic dish (8.5m in diameter)
Gain	45.8 ($\pm$0.3) dB
Beamwidth	0.9^o
Maximum Sidelobe	-27 dB (in any ϕ plane)
Rotational Rate	18°/sec
Scan types	PPI (optional sector scan), RHI, fixed-pointing, vertically pointing
Sidelobe	less than -27 dB

3.5. VOLUME MATCHING BETWEEN SPACE BASED AND GROUND BASED RADAR

Direct inter-comparisons between the GPM-DPR and ground radar is not possible because of the different viewing geometry of the two systems. The space based radar is a nadir pointing radar while ground based radars scan in PPI or RHI mode. For point by point comparisons, errors can crop in from observation resolution volume mismatch, spatial alignment and difference in operating frequency. The different observation geometry of the space and ground radar is shown in the picture 3.5.

It can be seen that the common resolution volume at the point of intersection of the two beams would be different. Several procedures have been proposed for volume matching and aligning space radar and ground radar by different researchers. The methodology by Bolen & Chandrasekar [10] is very widely used. It discusses the causes of distortion of the reflectivity map from space radar with respect to ground radar and its mitigation by resampling both the
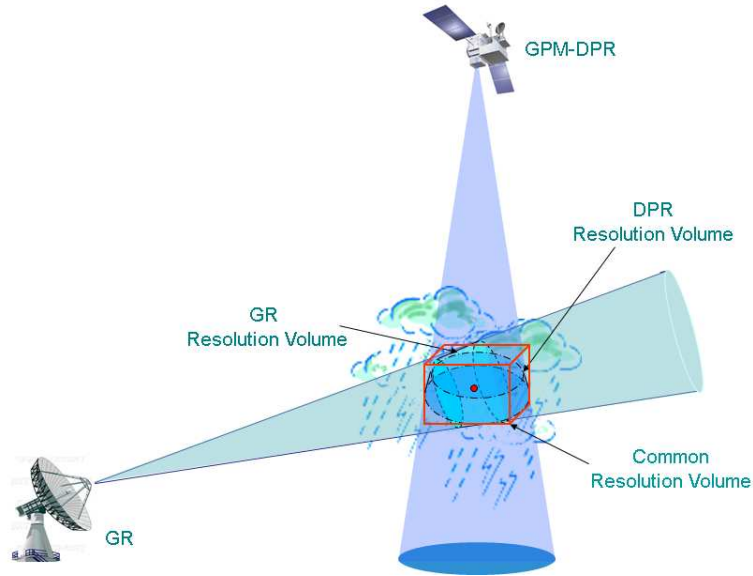
FIGURE 3.5. Viewing geometry of simultaneous observation of GPM-DPR and Ground Radar

reflectivity maps in a common grid by variable volume matching with a polynomial technique for alignment. Another approach proposed by Schwaller and Morris [2] performs the volume matching at each intersection points by averaging the range gates instead of resampling it into a new grid. It has been shown by the authors that this procedure causes less error due to interpolation as compared to the procedure described by Bolen & Chandrasekar [10]. A similar procedure has been followed in this work. First the location of intersection of the DPR's beam with GR's elevation sweeps is found out. The intersection points considered for volume matching should lie within the 100 Km range radius of the ground radar. This is because at ranges beyond 100 Km the ground radar beam widens greater than 2 Km and also due to atmospheric refraction the beam bends. Due to these issues ground radar data points beyond 100 Km would not provide any meaningful comparisons. The resolution or width of each range gate of the DPR's beam is 125 m. The horizontal footprint resolution

of the DPR's beam is 5 Km. Where as the gate width of typical S-band ground radar varies

between 250m to 150m. A cartoon depicting the common intersected gates is shown in 3.6.
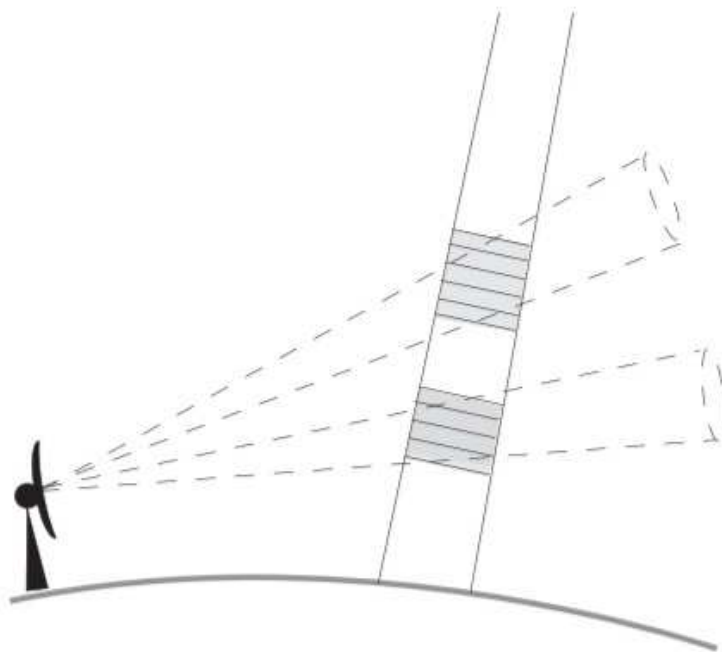
FIGURE 3.6. Cartoon showing DPR and GR gates at common intertection
locations for different GR sweeps. Image taken from [2]

Thus, at the intersection points the DPR gates falling between the beam width of the

GR are averaged vertically to match the GR beamwidth at that location. While, the number

of range gates falling within the footprint of the DPR beam are averaged to match 5 Km

resolution. In this way, the vertical resolution of DPR data is decreased and the horizontal

resolution of GR data is decreased. This procedure produces a output which is a set of vertical

profiles aligned along the DPR beam where samples points are located at the intersection

of GR sweep with DPR beam. All the GR observables are averaged in the same procedure.

Before averaging, only the reflectivity factor is converted to linear scale. It is again converted

back to logarithmic scale after averaging. Rainfall rates are also averaged in the similar way.

The average in case of DPR reflectivities at Ka band Ku band are simply arithmetic average whereas for GR, the various observables are averaged with a inverse weighting function.

CHAPTER 4

Comparison of observations and products between

GPM-DPR and Ground Radar

4.1. Comparison of Radar Reflectivity

In this chapter, observations from polarimetric S-band ground radar have been used to compare against the observations from GPM-DPR. S-Band radars are chosen because at this frequency the electromagnetic wave does not suffer significant or no attenuation while passing through precipitation media. The measured GR reflectivity is compared against the attenuation corrected reflectivity from DPR's Ku band $Z_e(Ku)$ and Ka band $Z_e(Ka)$. Here the symbol 'e' stands for effective. Reflectivity at these two frequencies suffers a lot of attenuation. Thus the measured reflectivities namely $Z_m(Ku)$ and $Z_m(Ka)$ are not used in the comparison. Several case studies are done when the DPR and GR had simultaneous observations of significant precipitation events. The cases studies are all based on S-Band NEXRADs, CSU-CHILL radar and NASA N-POL radar. 8 such case studies are presented in this chapter. A map of USA containing the locations of these different radars is shown below 4.1.

4.1.1. Case Studies. The first case study that is presented here is with the NEXRAD KFWS located at Dallas - Fort-Worth in Texas on 3rd March, 2015. The DPR's closest time of approach to the ground radar's location is 08:56:09 UTC. First the volume matching procedure as described in the previous chapter is performed before proceeding with any kind of comparisons. In figure 4.2 volume matched reflectivity is shown from DPR's Ku band, Ka band and GR's S band at 2Km and 4 Km height from above MSL.

FIGURE 4.1. Location of S-Band radars in the USA used in this GPM ground validation study

The outer black circle corresponds to 100 Km range radius and the inner one corresponds to 50 Km range radius of the GR. The black lines indicate GPM outer swath whereas the dotted lines indicate GPM inner swath. The solid red line is the NADIR. It should be noted that the swath width of Ka band is narrower (125 Km) than the outer Ku band swath (245 Km). It can be observed from the above figure 4.2 that the type of precipitation event observed is a quite wide spread stratiform case. Next, scatter plots have been shown to give an account of how well reflectivities are matched.

In the figure 4.3, samples from all the elevation have been considered while calculating the scatter plot. The red solid line is the 1:1 line while dotted lines represent ± 3 dBZ. As a measurement metric Bias and Standard Error (SE) have been calculated. Bias is defined as the mean of the differences between DPR - GR reflectivity samples. Standard Error is
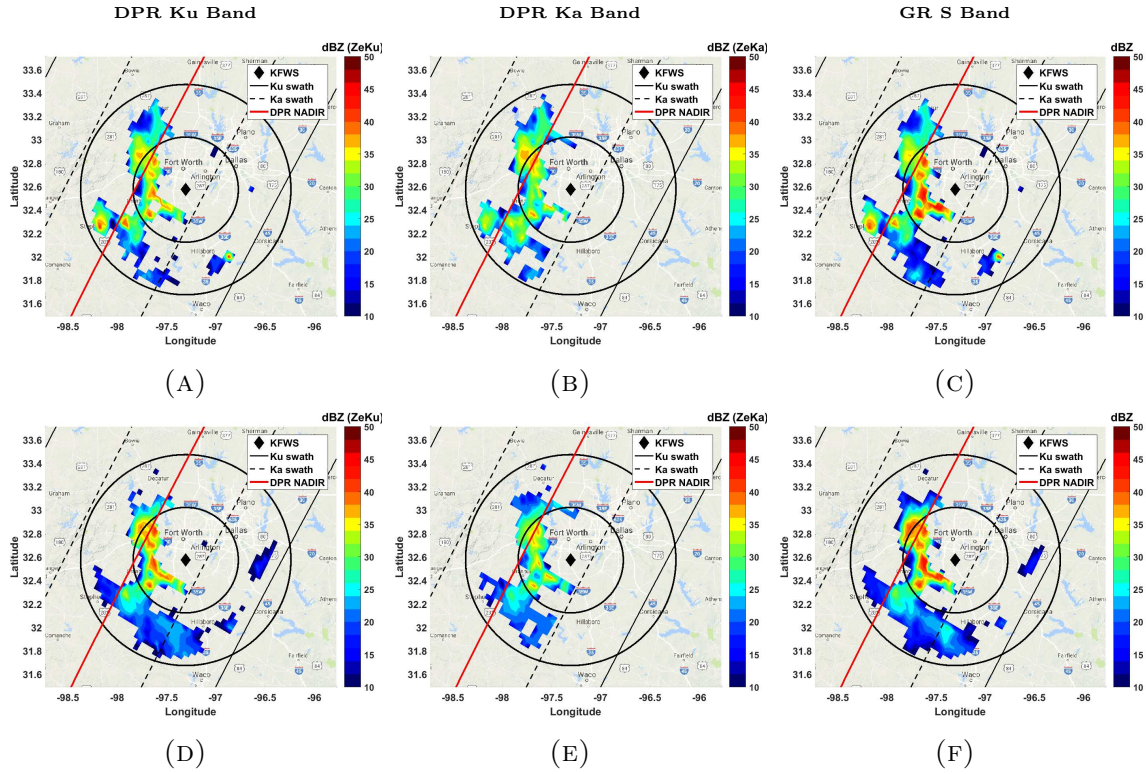
FIGURE 4.2. Volume matched reflectivity from DPR overpass with NEXRAD KFWS on 3rd March, 2015 at 08:56:09 UTC. (A) DPR $Z_e(Ku)$ at 2Km (B) DPR $Z_e(Ka)$ at 2Km (C) GR Z at 2Km (D) DPR $Z_e(Ku)$ at 4Km (E) DPR $Z_e(Ka)$ at 4Km (F) GR Z at 4Km
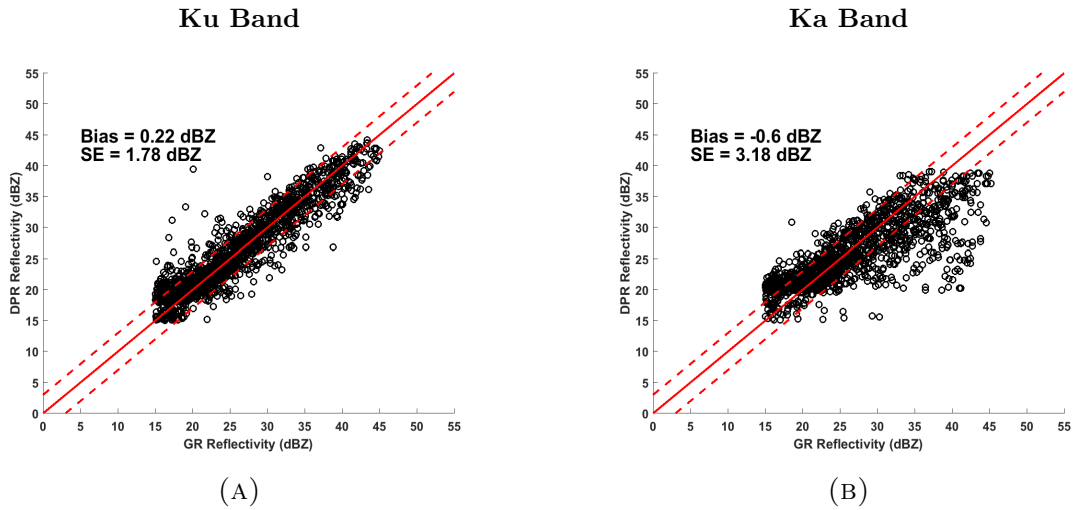
FIGURE 4.3. Scatter plot of DPR attenuation corrected reflectivity vs KFWS measured reflectivity for all samples from 3rd March, 2015 overpass case. (A) DPR $Z_e(Ku)$ vs GR Z (B) DPR $Z_e(Ka)$ vs GR Z

34

defined as the absolute of mean of DPR - GR samples. Mathematically they can be written as

$$Bias = \frac{1}{N} \sum_{n=1}^{N} (Z_{DPR} - Z_{GR}) \qquad (16)$$

$$SE = \frac{1}{N} \left| \sum_{n=1}^{N} (Z_{DPR} - Z_{GR}) \right| \qquad (17)$$

It can be seen that the Ku Band reflectivity bias is 0.22 dBZ and it increases on the negative side for the Ka band which is -0.6 dBZ. This increase can be accounted for the not so well performing attenuation correction algorithm at Ka band as compared to the Ku band. The standard errors for both cases are within a limit of 3 dBZ. The Profile Classification Module of the GPM-DPR Level 2 algorithm is capable of classifying the vertical profiles into stratiform and convective type [19]. In the inner swath a dual frequency method [20] is applied where both Ku and Ka band data are available. In the outer swath, Ku band being the only available data, a single frequency approach [19] is applied to get the type of precipitation. This information is used to classify the volume matched samples into stratiform and convective type. These samples are further classified into samples above and below the Bright Band. Mean bright band height information is again taken from DPR's profile classification output. A detail description on detection of bright band height is explained in Chapter 5. The samples are separated in this way as to get a deeper insight of how well the reflectivities are matched. For convective case the Ku and Ka band suffers more attenuation than compared to stratiform case. Also, above bright band, the attenuation is

significantly less due to the presence of ice particles. Below bright band, due to rain medium, both Ku and Ka band suffers significant attenuation. This can be observed in a typical vertical profile structure as observed by the DPR. Scatter plots of samples classified by rain types and separated by mean bright band height is presented in figure 4.4 for this case.

FIGURE 4.4. Scatter plot of DPR attenuation corrected Ku band vs KFWS measured reflectivity for samples classified into rain types from 3rd March, 2015 overpass case. (A) Stratiform samples above mean BB height. (B) Convective samples above mean BB height. (C) Stratiform samples below mean BB height. (D) Convective samples below mean BB height.

Stratiform, above BB

Convective, above BB

Stratiform, below BB

Convective, below BB
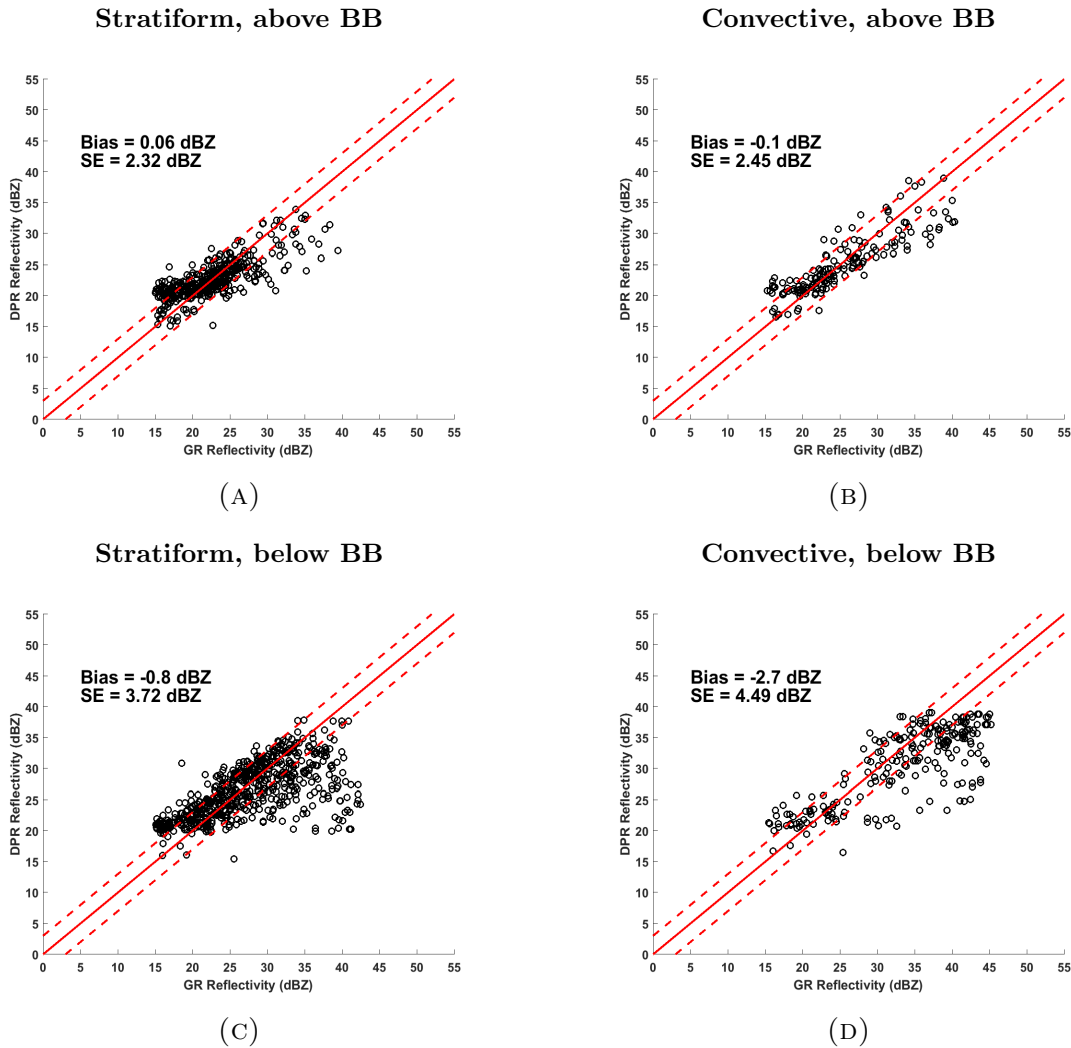
FIGURE 4.5. Scatter plot of DPR attenuation corrected Ka band vs KFWS measured reflectivity for samples classified into rain types from 3rd March, 2015 overpass case. (A) Stratiform samples above mean BB height. (B) Convective samples above mean BB height. (C) Stratiform samples below mean BB height. (D) Convective samples below mean BB height.

Biases and Standard Errors (SE) for different categories have been summarized below in table 4.1. It can be observed that although the biases lie around 0 dBZ, the SE for both stratiform and convective types increases from samples occurring above BB to samples occurring below BB indicating the effect of attenuation suffered at Ku and Ka bands in presence of rain.

TABLE 4.1. Table showing Bias and Standard Error for reflectivity comparison between DPR and KFWS of different precipitation types

	Ku Band				Ka Band			
	Stratiform		Convective		Stratiform		Convective	
	Bias (dBZ)	SE (dBZ)	Bias (dBZ)	SE (dBZ)	Bias (dBZ)	SE (dBZ)	Bias (dBZ)	SE (dBZ)
Above BB	0.51	1.66	0.39	1.63	0.06	2.32	-0.1	2.45
Below BB	0.01	1.94	0.12	2.15	-0.8	3.72	-2.7	4.49

Lastly, volume matched vertical profile of reflectivity is compared from both the radars. Figure 4.6 shows two vertical profiles at location A and B. Corresponding vertical cuts have also been shown. The reflectivity profiles at Ku and S Band are quite well matched. The Ka band profile matches for case B while for case A it is not that case. The profile at A is a stratiform one and that at B is a convective one. When the attenuation suffered is quite significant due to heavy convection, the GPM attenuation correction algorithm sometimes can change the measured reflectivity by a factor of 10 [13]. This can be the reason for well matching of the Ka band in case B. Other dual-polarization observables from GR are also presented, which includes Z_{dr}, ρ_{hv} and K_{dp}, to get an idea of the microphysics of the vertical profiles.

In early August 2016, a mesoscale convective system developed over Louisiana, USA which caused torrential rain and flooding. The system formed around a weak area of low pressure and it remained stationary over the southern region of Louisiana for few days due to which heavy rainfall occurred measuring up to 3 inches an hour. This whole event continued for few days starting from August 11th, 2016. In this case study, observations of this event from both ground radar KLIX and DPR have been analyzed and made to compare against each other for validation. On 12th August 2016 GPM-DPR made an overpass with NEXRAD KLIX located at New Orleans, Louisiana. The closest time of approach was 12:16:44 UTC.

FIGURE 4.6. Volume matched vertical profile of reflectivity comparison between from DPR overpass with NEXRAD KFWS on 3rd March, 2015 at 08:56:09 UTC. (A) DPR $Z_e(Ku)$ at 2Km showing VP location (B) Vertical Cut of reflectivity at A (C) Vertical Cut of reflectivity at B (D) Vertical profiles at A (E) Vertical Profiles at B

In figure 4.7 volume matched reflectivity is shown from DPR's Ku band, Ka band and GR's S band at 2Km and 4 Km height from above MSL.
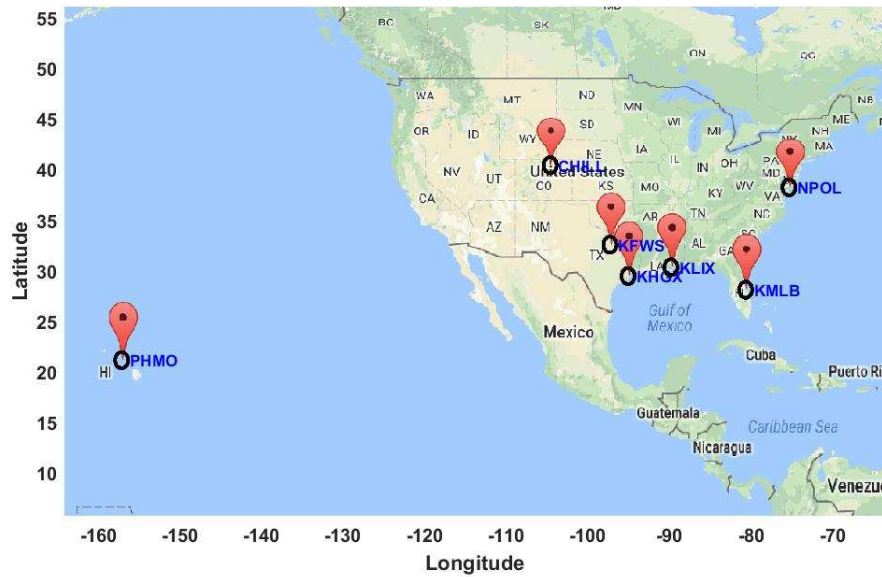
The outer black circle corresponds to 100 Km range radius and the inner one corresponds to 50 Km range radius of the GR. The black lines indicate GPM outer swath whereas the dotted lines indicate GPM inner swath. The solid red line is the NADIR. Next, scatter plots have been shown to give an account of how well reflectivities are matched.

FIGURE 4.7. Volume matched reflectivity from DPR overpass with NEXRAD KLIX on 12th August, 2016 at 12:16:44 UTC. (A) DPR $Z_e(Ku)$ at 2Km (B) DPR $Z_e(Ka)$ at 2Km (C) GR Z at 2Km (D) DPR $Z_e(Ku)$ at 4Km (E) DPR $Z_e(Ka)$ at 4Km (F) GR Z at 4Km

FIGURE 4.8. Scatter plot of DPR attenuation corrected reflectivity vs KLIX measured reflectivity for all samples from 12th August, 2016 overpass case. (A) DPR $Z_e(Ku)$ vs GR Z (B) DPR $Z_e(Ka)$ vs GR Z

TABLE 4.2. Table showing Bias and Standard Error for reflectivity comparison between DPR and KLIX of different precipitation types

	Ku Band				Ka Band			
	Stratiform		Convective		Stratiform		Convective	
	Bias (dBZ)	SE (dBZ)	Bias (dBZ)	SE (dBZ)	Bias (dBZ)	SE (dBZ)	Bias (dBZ)	SE (dBZ)
Above BB	0.43	1.45	0.93	2.06	-0.37	3.83	0.2	2.12
Below BB	1.04	1.79	0.72	2.09	0.31	1.35	-0.7	1.54

In the figure 4.8, samples from all the heights have been considered. The red solid line is the 1:1 line while dotted lines represent ±3 dBZ. The Ku Band reflectivity bias is 0.84 dBZ. It increases on the negative side for the Ka band which is -0.9 dBZ. This same trend like the previous case study with KFWS increase can be accounted for the GPM's attenuation correction algorithm at Ka band. The standard errors for both cases are within a limit of 3 dBZ which is a good agreement. Finally, scatter plots of samples classified by rain types and separated by mean bright band height is presented in figures 4.9 and 4.10 for this case. The mean bright band height for this case has been found to be 4600 m.

Biases and Standard Errors (SE) for different categories have been summarized below in table 4.2. It is interesting to note here, that although the general trend for SE is to increase from above bright band height to below bright band height for convective samples, in this case for Ka band it decreases. It again can be due to the fact that the attenuation correction technique is changing the raw reflectivity by a huge factor.

Lastly, volume matched vertical profile of reflectivity is compared from both the radars. Figure 4.11 shows two vertical profiles at location A and B. Corresponding vertical cuts have been also shown. The reflectivity profiles at Ku and S and Ka Band are quite well matched.

Stratiform, above BB

Convective, above BB

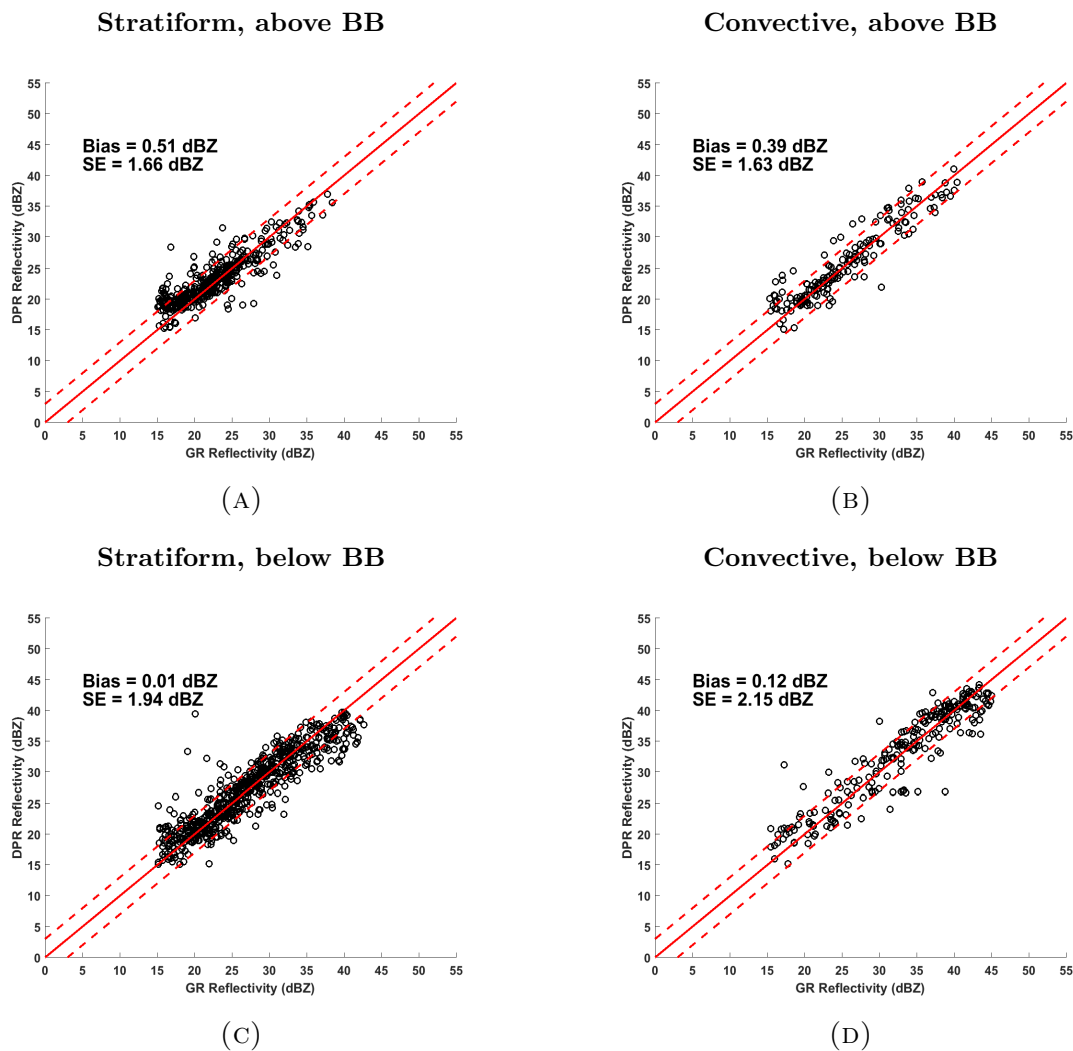**Stratiform, below BB**

Convective, below BB

(A) (B)

(C) (D)

FIGURE 4.9. Scatter plot of DPR attenuation corrected Ku band vs KLIX measured reflectivity for samples classified into rain types from 12th August, 2016 overpass case. (A) Stratiform samples above mean BB height. (B) Convective samples above mean BB height. (C) Stratiform samples below mean BB height. (D) Convective samples below mean BB height.

The profile at A is a convective one and that at B is a stratiform one. Other dual-polarization observables from GR are also presented, which includes Z_{dr}, ρ_{hv} and K_{dp}.

The third case study is an interesting case of GPM DPR overpass with Hurricane Ana on 19th October 2014, after its landfall at Molokai, Hawaii islands. The ground radar located at this place is NEXRAD PHMO. The closest time of DPR's approach with the GR is 18:48:12

Stratiform, above BB

Bias = -3.7 dBZ
SE = 3.83 dBZ

(A)

Convective, above BB

Bias = 0.20 dBZ
SE = 2.12 dBZ

(B)

Stratiform, below BB

Bias = 0.31 dBZ
SE = 1.35 dBZ

(C)

Convective, below BB

Bias = -0.7 dBZ
SE = 1.54 dBZ

(D)

FIGURE 4.10. Scatter plot of DPR attenuation corrected Ka band vs KLIX measured reflectivity for samples classified into rain types from 12th August, 2016 overpass case. (A) Stratiform samples above mean BB height. (B) Convective samples above mean BB height. (C) Stratiform samples below mean BB height. (D) Convective samples below mean BB height.

UTC. In figure 4.12 volume matched reflectivity is shown from DPR's Ku band, Ka band and GR's S band at 2Km and 4 Km height from above MSL.

The outer black circle corresponds to 100 Km range radius and the inner one corresponds to 50 Km range radius of the GR. The black lines indicate GPM outer swath whereas the
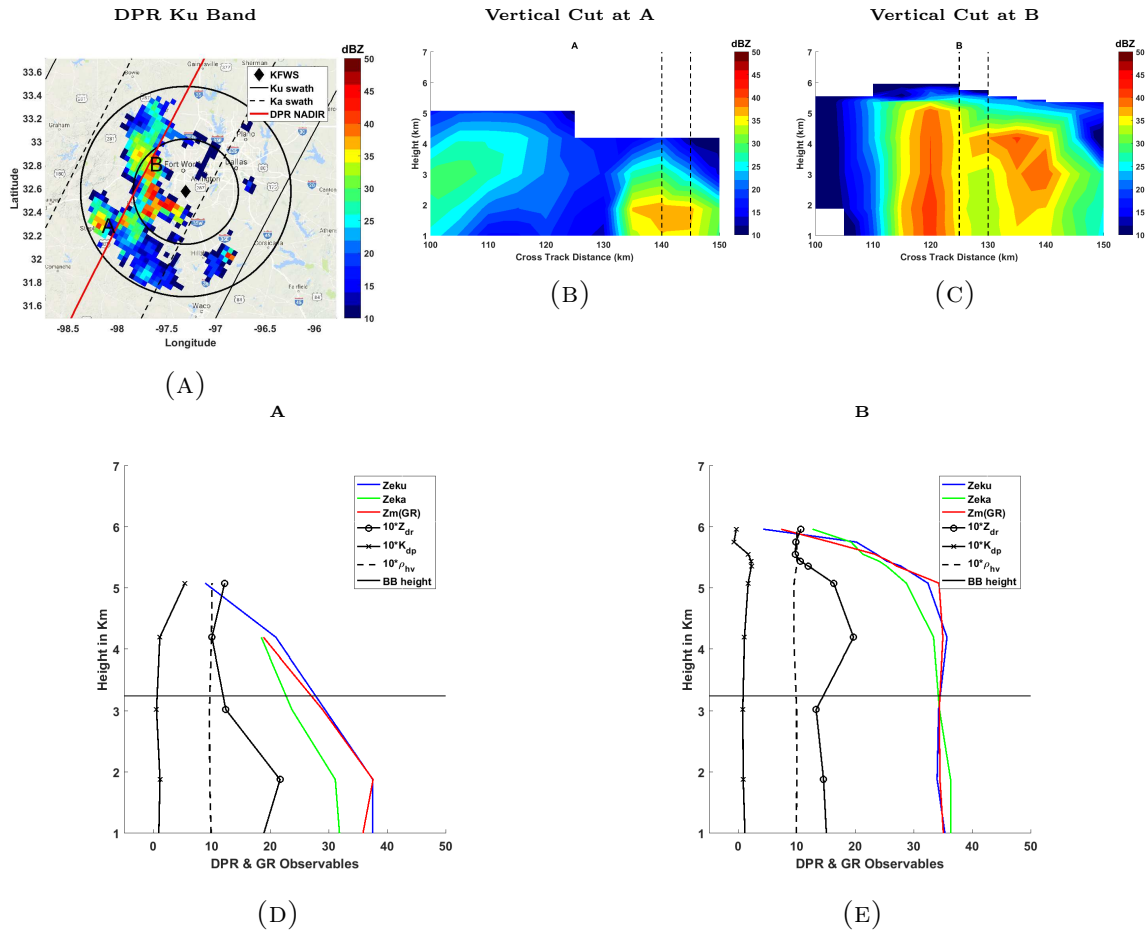
FIGURE 4.11. Volume matched vertical profile of reflectivity comparison between from DPR overpass with NEXRAD KLIX on 12th August, 2015 at 12:16:44 UTC. (A) DPR $Z_e(Ku)$ at 2Km showing VP location (B) Vertical Cut of reflectivity at A (C) Vertical Cut of reflectivity at B (D) Vertical profiles at A (E) Vertical Profiles at B

dotted lines indicate GPM inner swath. The solid red line is the NADIR. Next, scatter plots have been shown to give an account of how well reflectivities are matched.
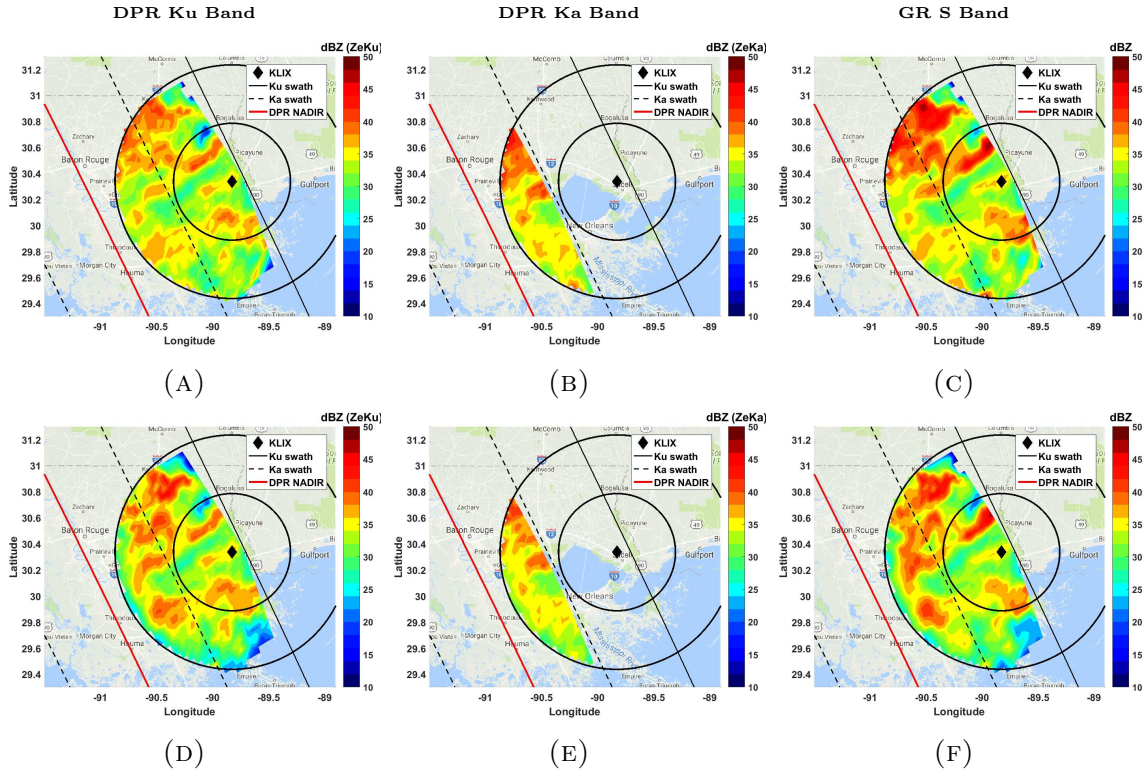
In the figure 4.13, samples from all the heights have been considered. The red solid line is the 1:1 line while dotted lines represent ± 3 dBZ. Looking at the bias and standard error it can be said that both Ku and Ka band are in good agreement with the GR. The SE for both cases lies within 2 dBZ roughly. Scatter plots of samples classified by rain types and

FIGURE 4.12. Volume matched reflectivity from DPR overpass with NEXRAD PHMO on 19th October, 2014 at 18:42:12 UTC. (A) DPR $Z_e(Ku)$ at 2Km (B) DPR $Z_e(Ka)$ at 2Km (C) GR Z at 2Km (D) DPR $Z_e(Ku)$ at 4Km (E) DPR $Z_e(Ka)$ at 4Km (F) GR Z at 4Km
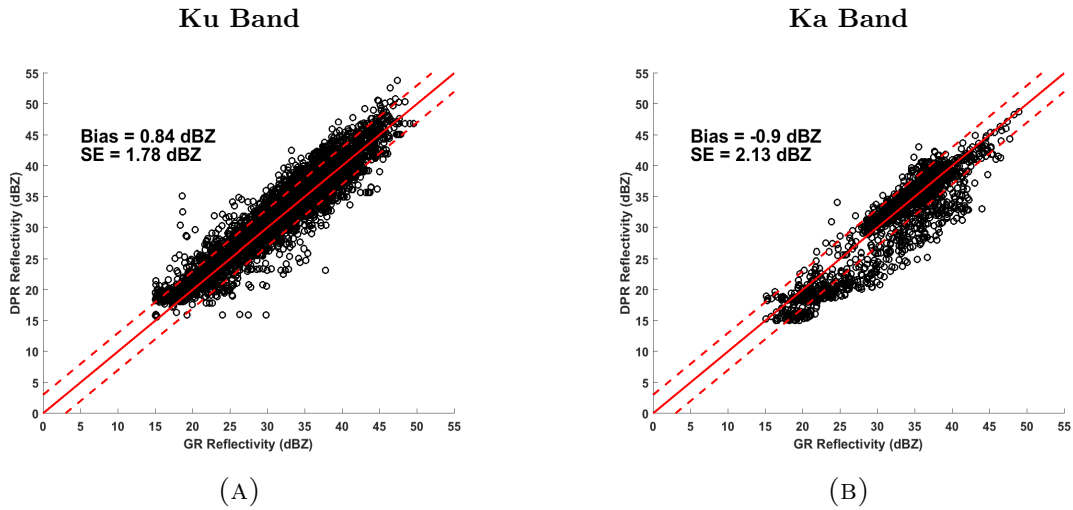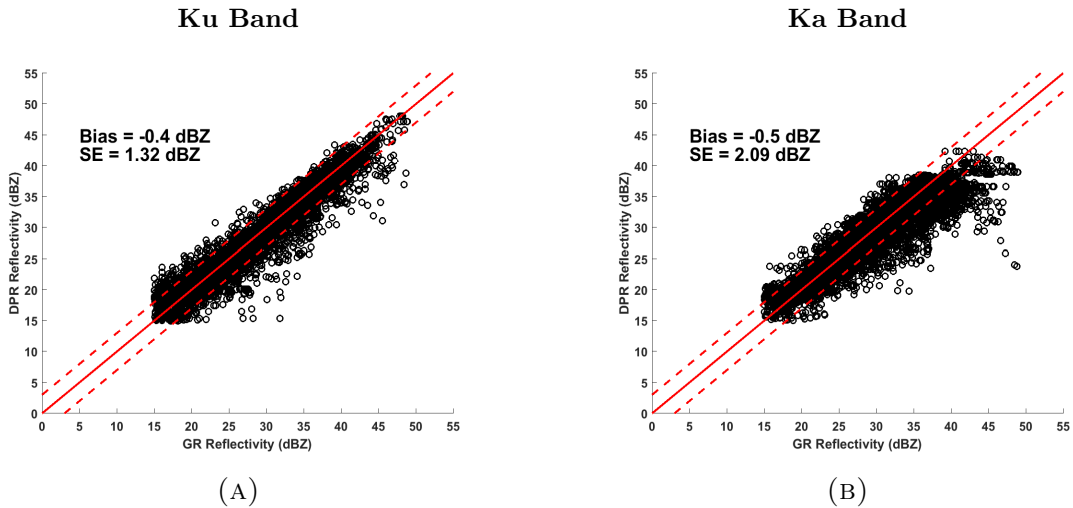

FIGURE 4.13. Scatter plot of DPR attenuation corrected reflectivity vs PHMO measured reflectivity for all samples from 19th October, 2014 overpass case. (A) DPR $Z_e(Ku)$ vs GR Z (B) DPR $Z_e(Ka)$ vs GR Z

separated by mean bright band height is presented in figures 4.14 and 4.15 for this case. The mean bright band height for this case has been found to be 4200 m.

Stratiform, above BB

(A)

Convective, above BB

(B)

Stratiform, below BB

(C)

Convective, below BB

(D)

FIGURE 4.14. Scatter plot of DPR attenuation corrected Ku band vs PHMO measured reflectivity for samples classified into rain types from 19th October, 2014 overpass case. (A) Stratiform samples above mean BB height. (B) Convective samples above mean BB height. (C) Stratiform samples below mean BB height. (D) Convective samples below mean BB height.

Biases and Standard Errors (SE) for different categories have been summarized in table 4.3.

Stratiform, above BB   **Convective, above BB**

Bias = -1.0 dBZ
SE = 2.04 dBZ

Bias = -0.8 dBZ
SE = 1.68 dBZ

(A)   (B)

Stratiform, below BB   **Convective, below BB**

Bias = -0.1 dBZ
SE = 1.91 dBZ

Bias = -2.8 dBZ
SE = 3.86 dBZ

(C)   (D)

FIGURE 4.15. Scatter plot of DPR attenuation corrected Ka band vs PHMO measured reflectivity for samples classified into rain types from 19th October, 2014 overpass case. (A) Stratiform samples above mean BB height. (B) Convective samples above mean BB height. (C) Stratiform samples below mean BB height. (D) Convective samples below mean BB height.

TABLE 4.3. Table showing Bias and Standard Error for reflectivity comparison between DPR and PHMO of different precipitation types

	Ku Band				Ka Band			
	Stratiform		Convective		Stratiform		Convective	
	Bias (dBZ)	SE (dBZ)	Bias (dBZ)	SE (dBZ)	Bias (dBZ)	SE (dBZ)	Bias (dBZ)	SE (dBZ)
Above BB	0.23	1.3	0.40	1.12	-1	2.04	-0.8	1.68
Below BB	-0.5	1.31	-0.5	1.42	-0.1	1.91	-2.8	3.86

Lastly, volume matched vertical profile of reflectivity is compared from both the radars.

Figure 4.16 shows two vertical profiles at location A and B. Corresponding vertical cuts have

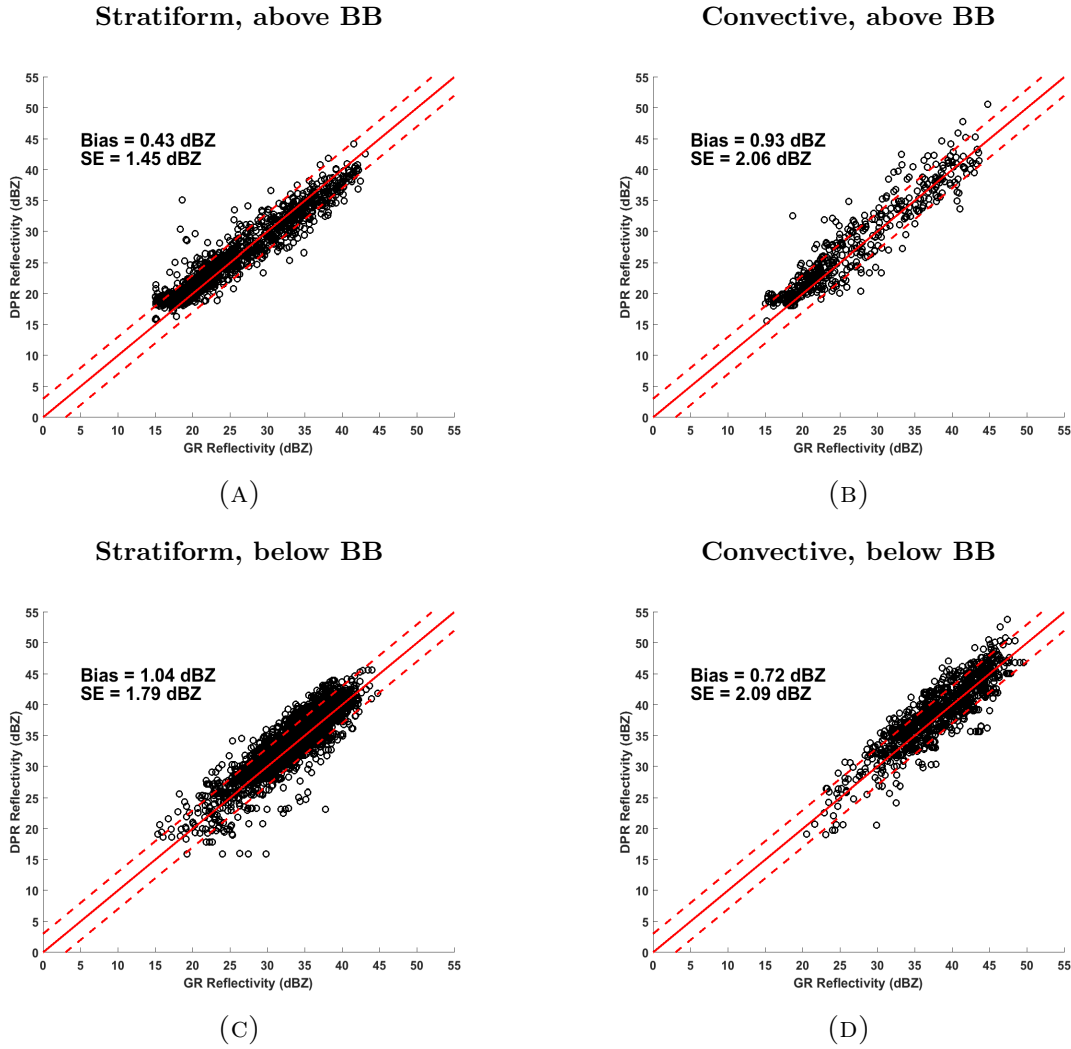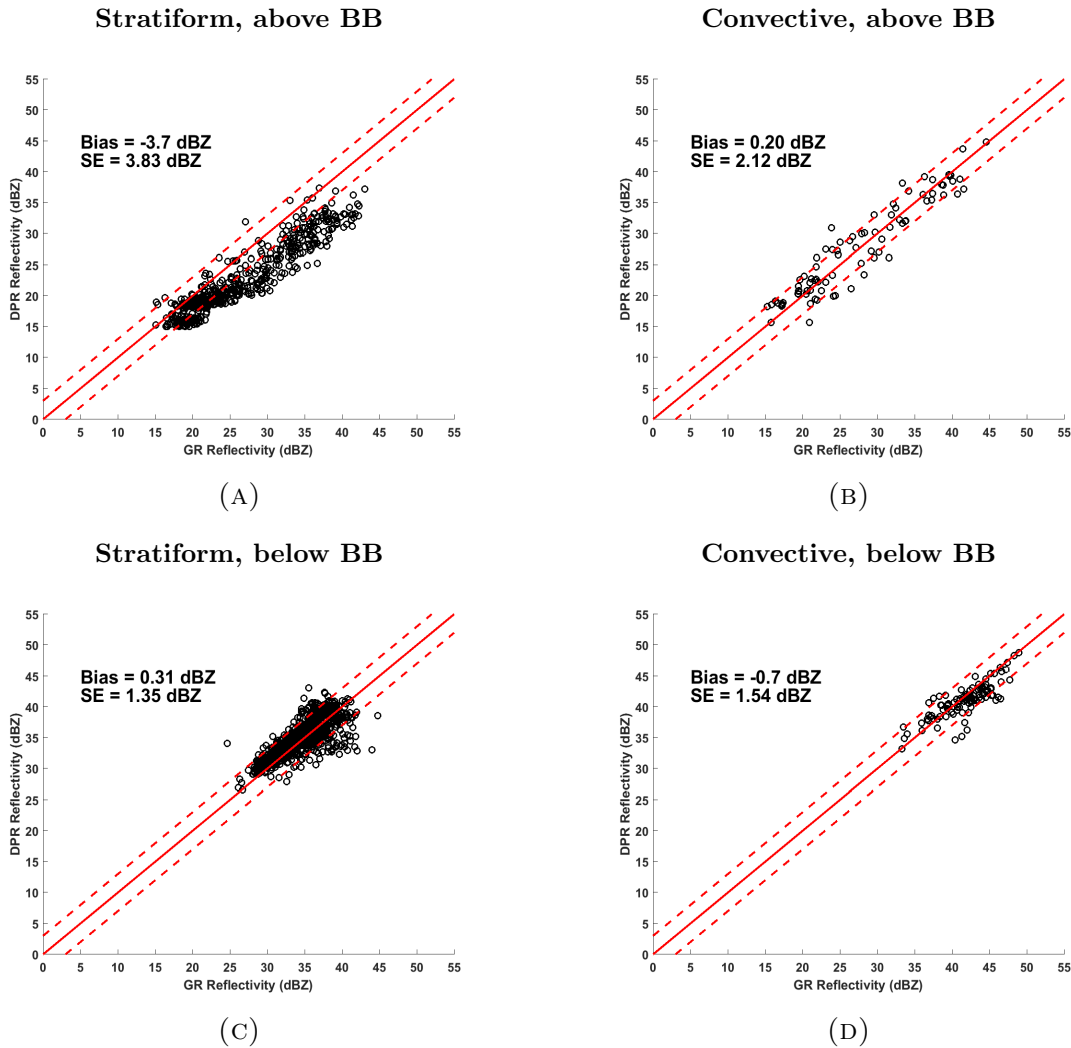been also shown. The reflectivity profiles at Ku and S and Ka Band are quite well matched. The profile at A is a convective one and that at B is a stratiform one. Other dual-polarization observables from GR are also presented, which includes Z_{dr}, ρ_{hv} and K_{dp}.
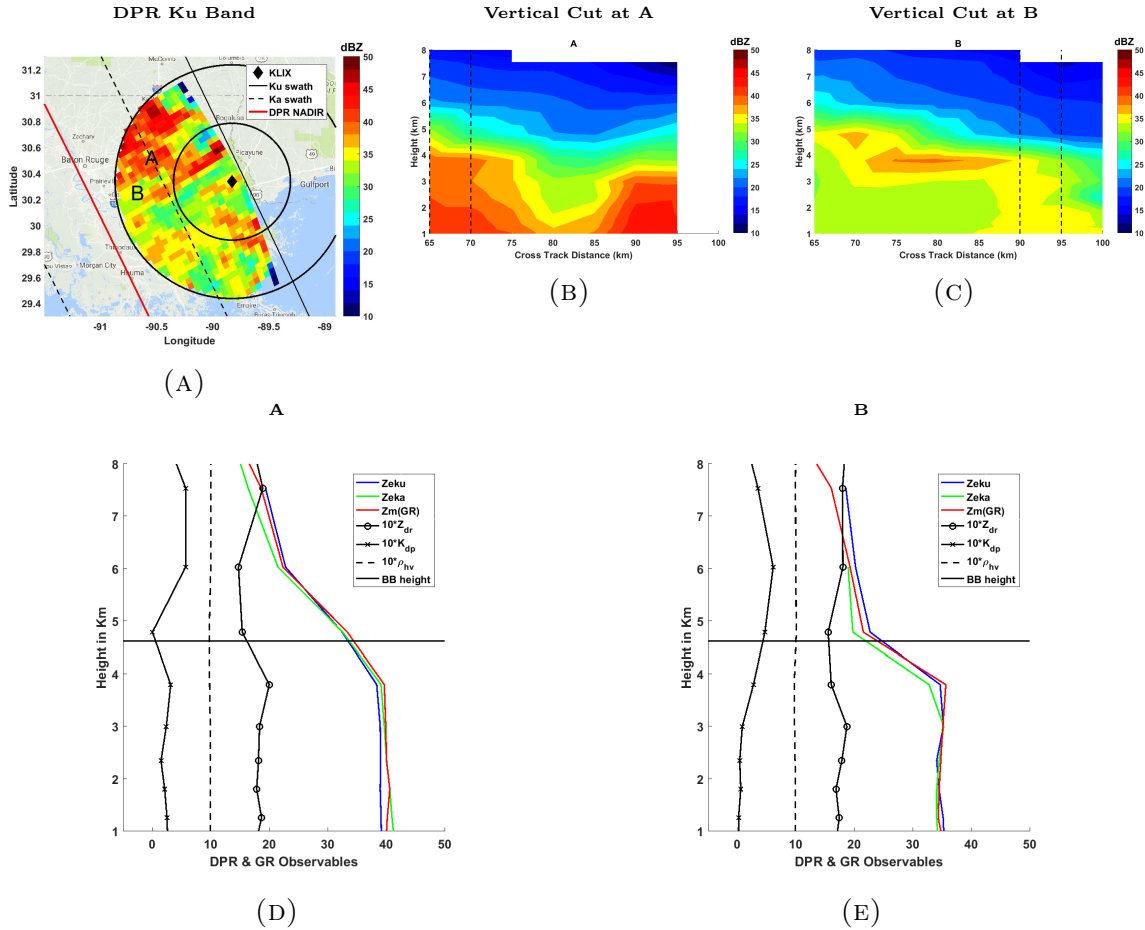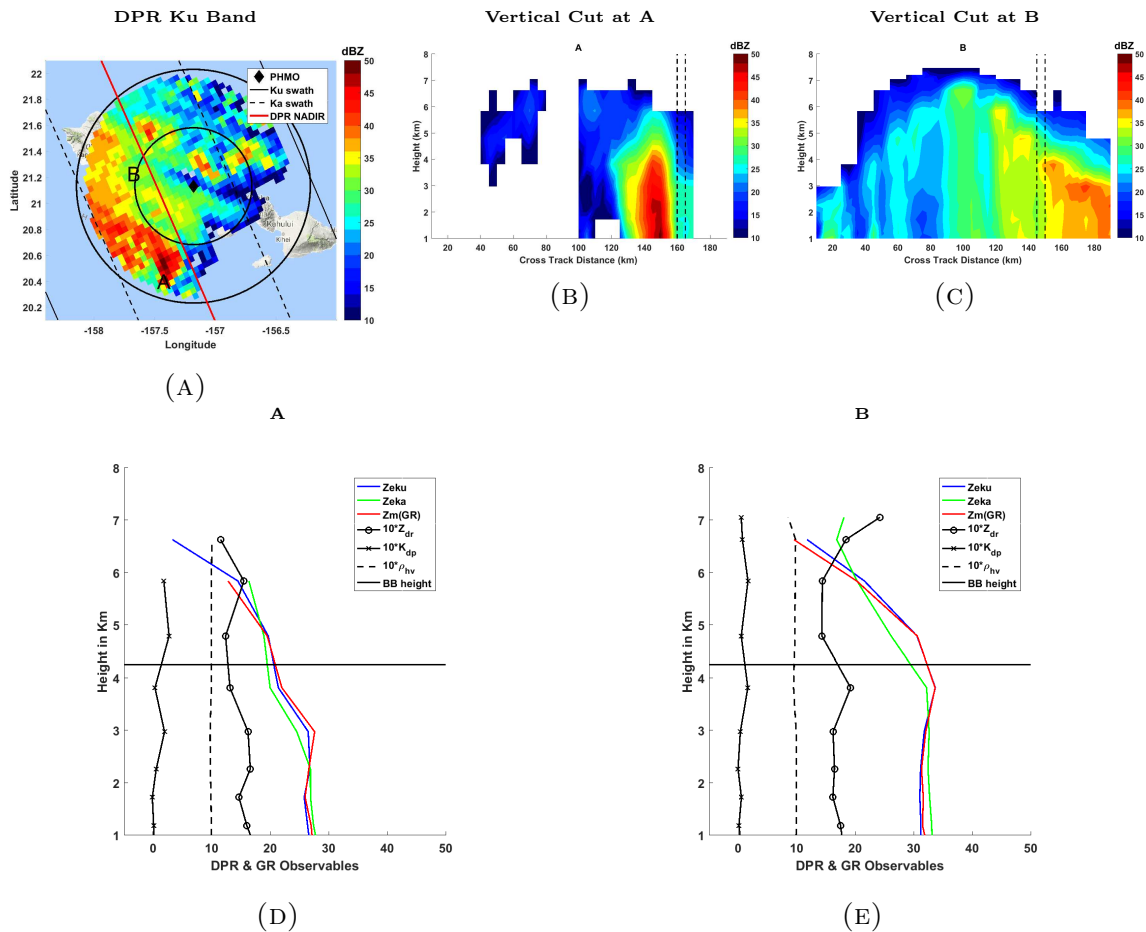

FIGURE 4.16. Volume matched vertical profile of reflectivity comparison between from DPR overpass with NEXRAD PHMO on 19th October, 2014 at 18:48:12 UTC. (A) DPR $Z_e(Ku)$ at 2Km showing VP location (B) Vertical Cut of reflectivity at A (C) Vertical Cut of reflectivity at B (D) Vertical profiles at A (E) Vertical Profiles at B

The last case study presented here is a GPM Oveerpass with CSU-CHILL radar on 17th August 2015. The closest time of approach for this case was 21:59:07 UTC. In figure 4.17
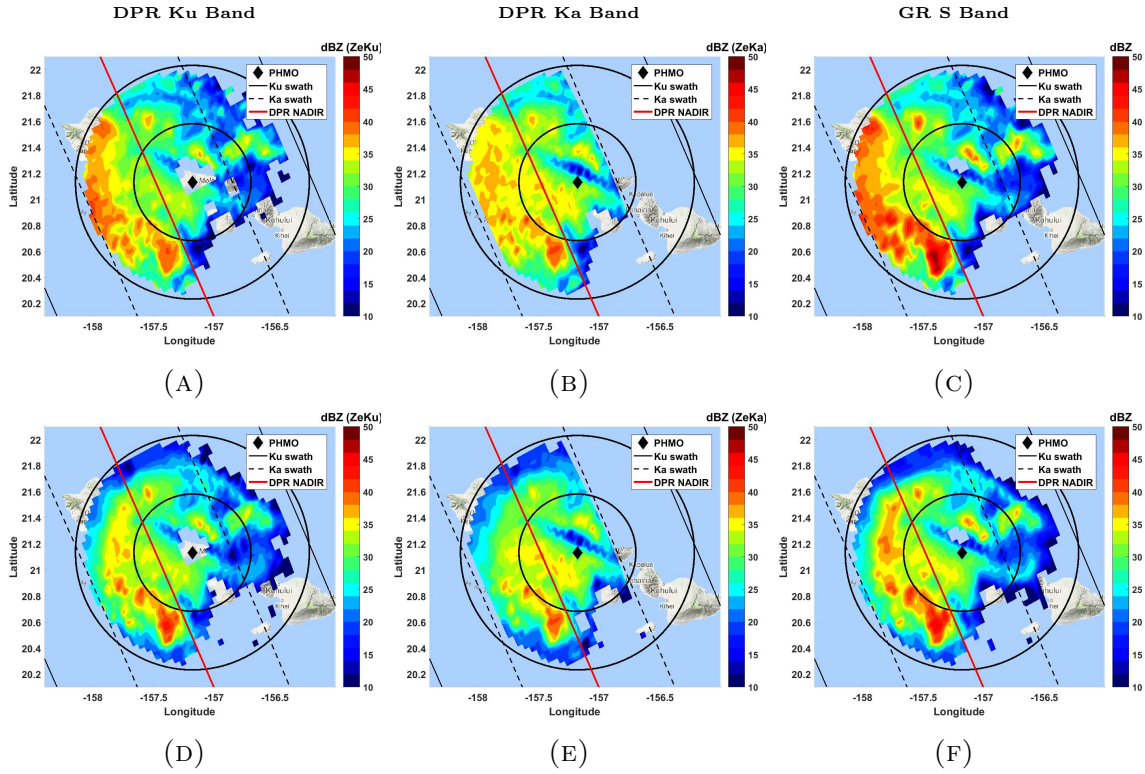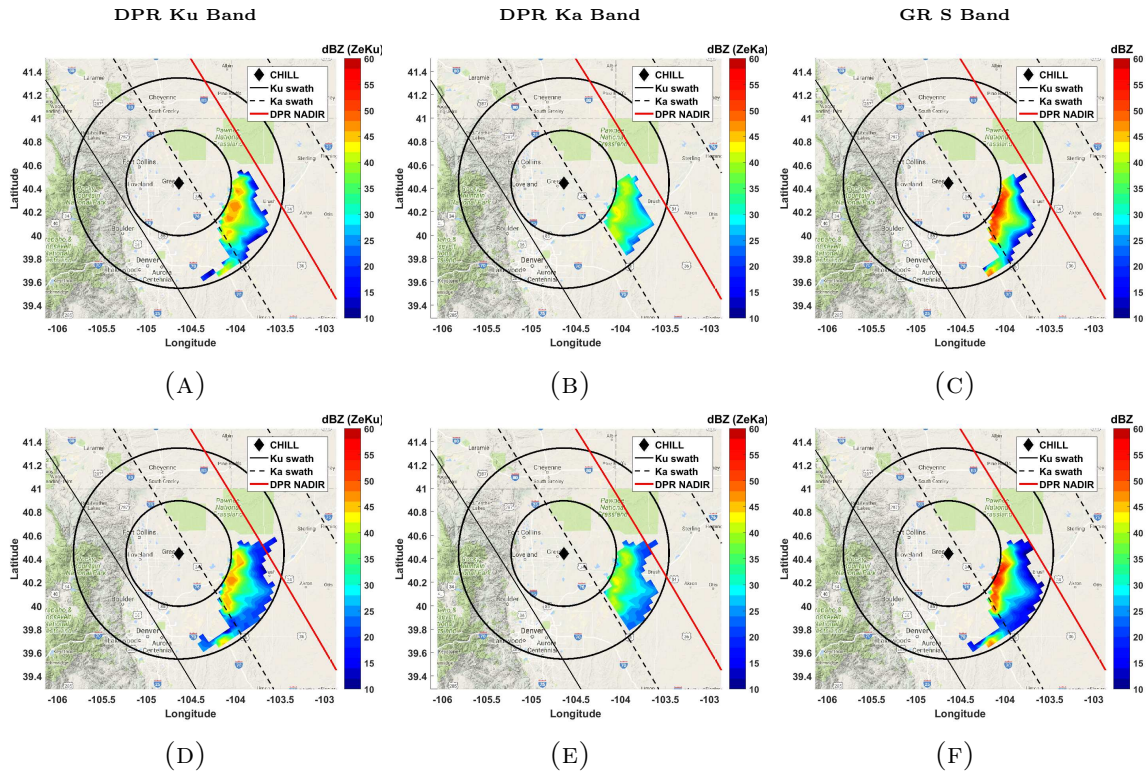
FIGURE 4.17. Volume matched reflectivity from DPR overpass with NEXRAD CHILL on 17th August, 2015 at 21:57:12 UTC. (A) DPR $Z_e(Ku)$ at 2Km (B) DPR $Z_e(Ka)$ at 2Km (C) GR Z at 2Km (D) DPR $Z_e(Ku)$ at 4Km (E) DPR $Z_e(Ka)$ at 4Km (F) GR Z at 4Km

volume matched reflectivity is shown from DPR's Ku band, Ka band and GR's S band at 2Km and 4 Km height from above MSL.

The outer black circle corresponds to 100 Km range radius and the inner one corresponds to 50 Km range radius of the GR. The black lines indicate GPM outer swath whereas the dotted lines indicate GPM inner swath. The solid red line is the NADIR. From the plots in figure 4.17,it can be observed that the precipitation event is a strong convective cell with reflectivity values reaching upto 60 dBZ. Next, scatter plots have been shown to give an account of how well reflectivities are matched.

Ku Band

Bias = -0.6 dBZ
SE = 3.51 dBZ

Ka Band

Bias = -2.7 dBZ
SE = 5.97 dBZ

(A)   (B)
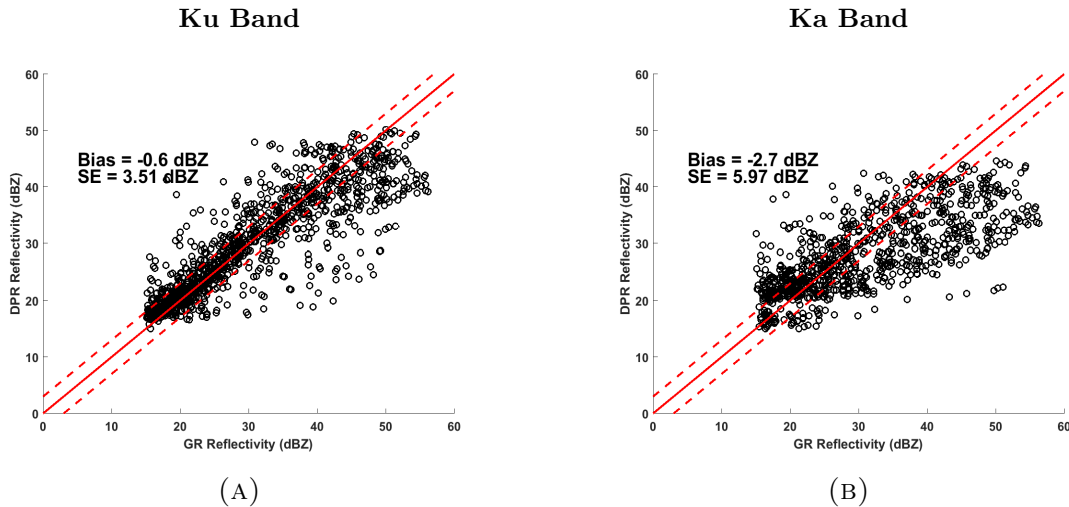
FIGURE 4.18. Scatter plot of DPR attenuation corrected reflectivity vs CHILL measured reflectivity for all samples from 17th August, 2015 overpass case. (A) DPR $Z_e(Ku)$ vs GR Z (B) DPR $Z_e(Ka)$ vs GR Z

In the figure 4.18, samples from all the heights have been considered. The red solid line is the 1:1 line while dotted lines represent ± 3 dBZ. Due to heavy convection, both Ku and Ka samples have suffered a large attenuation and this can be seen in the standard error. For Ku band it is close to 4 dBZ while it is as large as 6 dBZ in Ka band. Scatter plots of samples classified by rain types and separated by mean bright band height is presented in figures 4.19 and 4.20 for this case. The mean bright band height for this case has been found to be 5100 m.
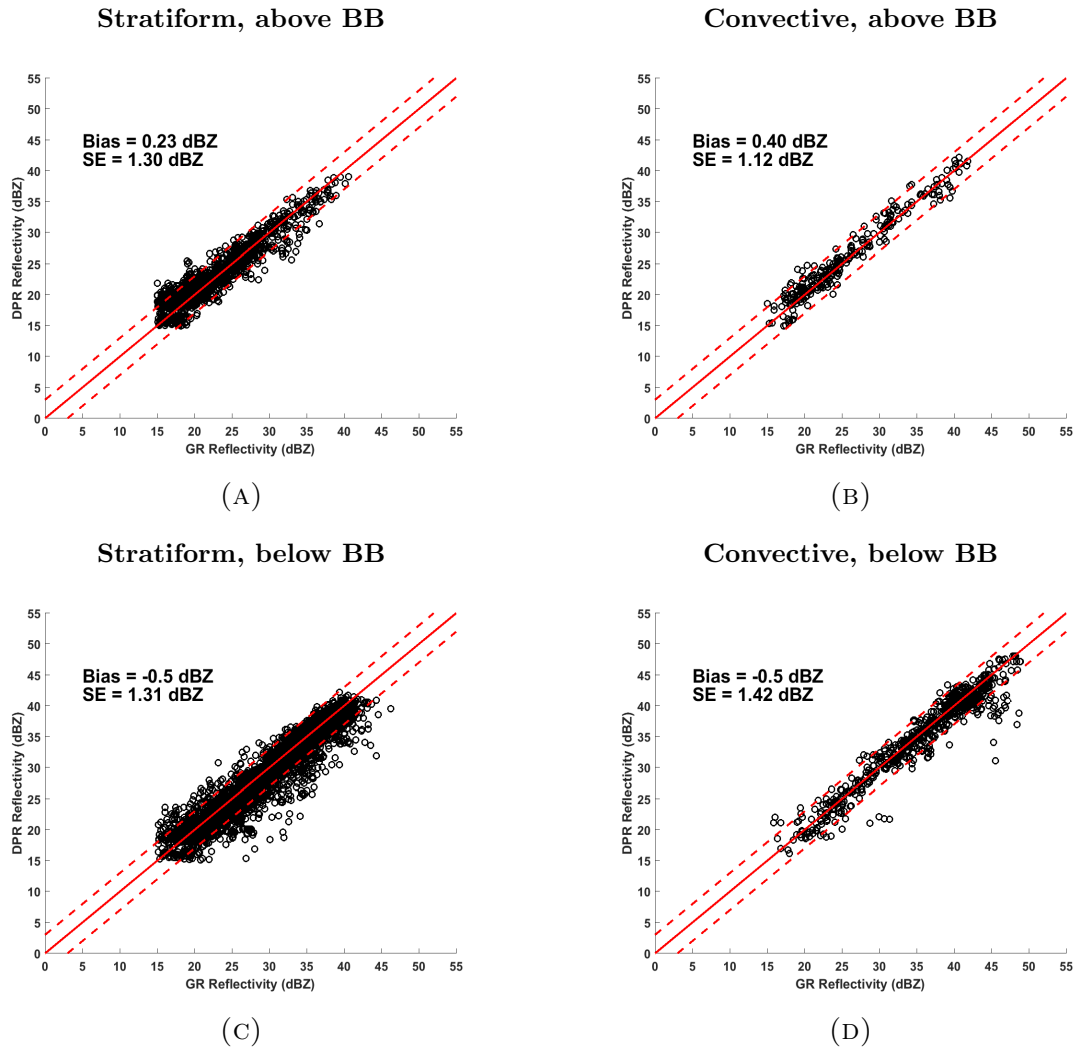
Biases and Standard Errors (SE) for different categories have been summarized in table 4.4. Lastly, volume matched vertical profile of reflectivity is compared from both the radars. Figure 4.21 shows two vertical profiles at location A and B. Corresponding vertical cuts have been also shown. The reflectivity profiles at Ku and S are well matched. The profile at A is a convective one. It can be seen the Ka band profile is not matched due heavy attenuation.

Stratiform, above BB

Bias = 0.22 dBZ
SE = 1.16 dBZ

(A)

Convective, above BB

Bias = -0.8 dBZ
SE = 2.52 dBZ

(B)

Stratiform, below BB

Bias = 1.20 dBZ
SE = 3.26 dBZ
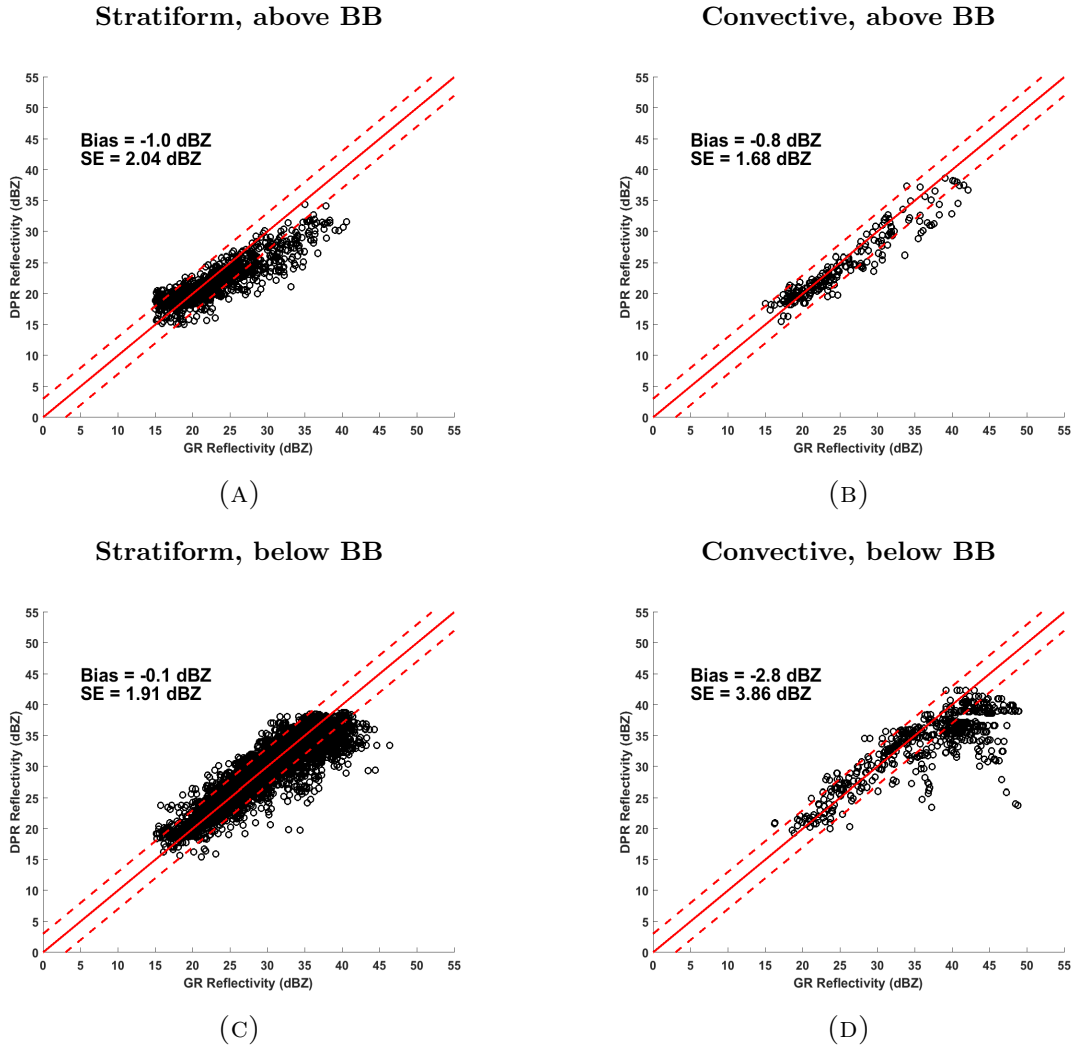
(C)

Convective, below BB

Bias = -1.6 dBZ
SE = 6.12 dBZ

(D)
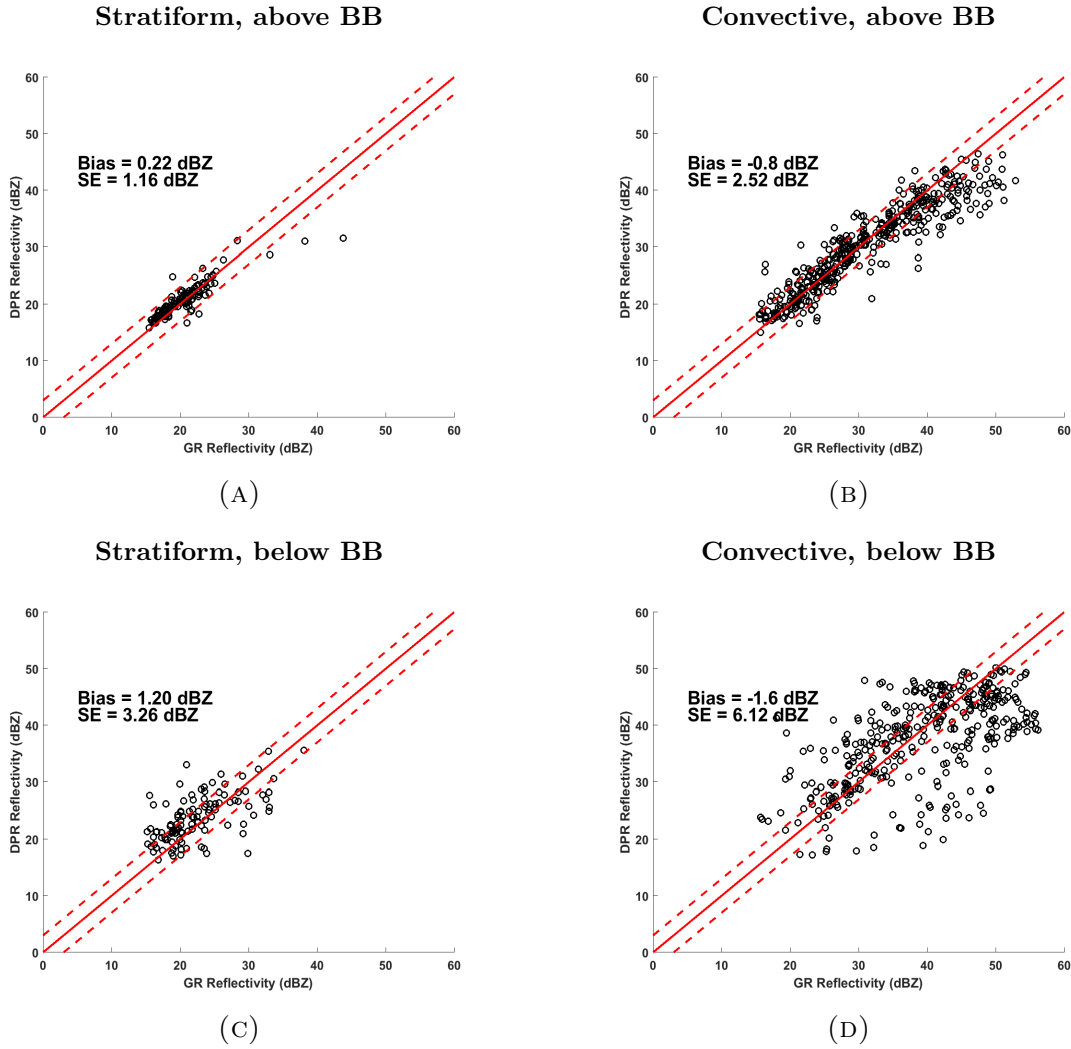
FIGURE 4.19. Scatter plot of DPR attenuation corrected Ku band vs PHMO measured reflectivity for samples classified into rain types from 17th August, 2015 overpass case. (A) Stratiform samples above mean BB height. (B) Convective samples above mean BB height. (C) Stratiform samples below mean BB height. (D) Convective samples below mean BB height.

TABLE 4.4. Table showing Bias and Standard Error for reflectivity comparison between DPR and CHILL of different precipitation types

	Ku Band				Ka Band			
	Stratiform		Convective		Stratiform		Convective	
	Bias (dBZ)	SE (dBZ)	Bias (dBZ)	SE (dBZ)	Bias (dBZ)	SE (dBZ)	Bias (dBZ)	SE (dBZ)
Above BB	0.22	1.16	-0.8	2.52	1.04	2.48	-5.8	6.29
Below BB	1.20	3.26	-1.6	6.12	5.32	5.40	-3.8	7.32

The Ka band profile at B which is a stratiform one matches well with Ku and S Band. Other dual-polarization observables from GR are also presented, which includes Z_{dr}, ρ_{hv} and K_{dp}.

Stratiform, above BB

Convective, above BB

(A)

(B)

Stratiform, below BB

Convective, below BB

(C)

(D)
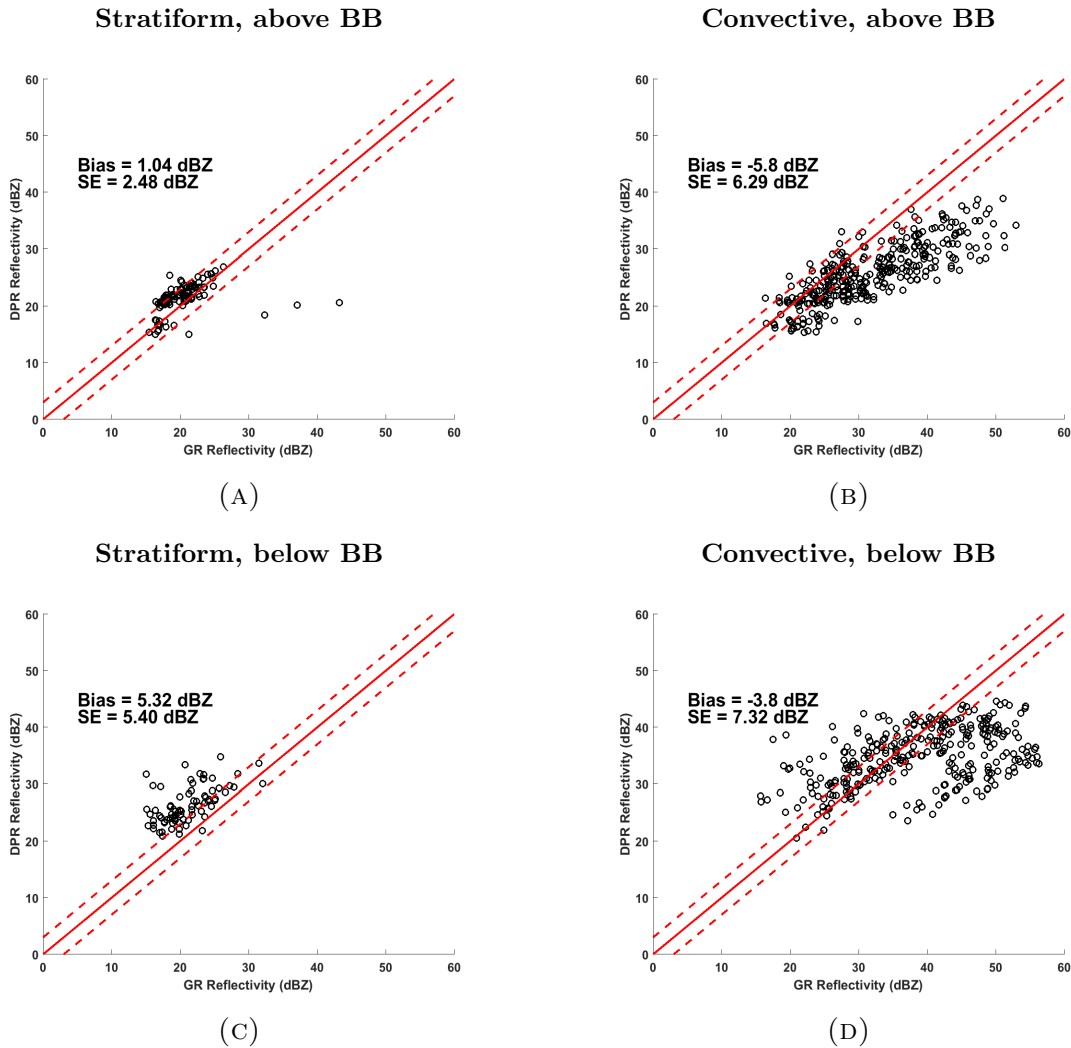
FIGURE 4.20. Scatter plot of DPR attenuation corrected Ka band vs CHILL measured reflectivity for samples classified into rain types from 17th August, 2015 overpass case. (A) Stratiform samples above mean BB height. (B) Convective samples above mean BB height. (C) Stratiform samples below mean BB height. (D) Convective samples below mean BB height.

4.2. TIME SERIES OF MEAN DPR-GR REFLECTIVITY BIASES

Mean reflectivity bias between the GPM DPR and GR is observed over the years since GPM launch till date. Four well calibrated NEXRADs are chosen for this study. Their name and location is shown in the table 4.5.
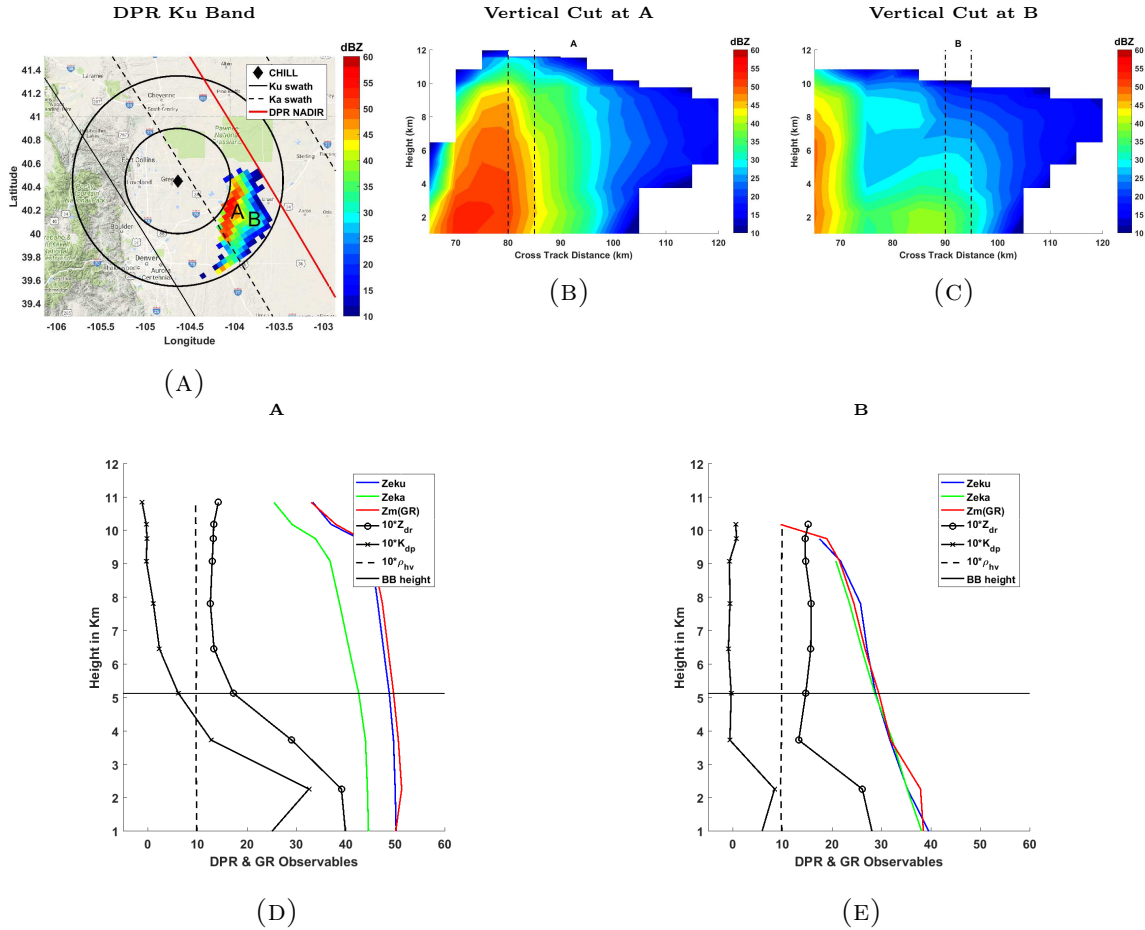
FIGURE 4.21. Volume matched vertical profile of reflectivity comparison between from DPR overpass with NEXRAD CHILL on 17th August, 2015 at 21:59:07 UTC. (A) DPR $Z_e(Ku)$ at 2Km showing VP location (B) Vertical Cut of reflectivity at A (C) Vertical Cut of reflectivity at B (D) Vertical profiles at A (E) Vertical Profiles at B

TABLE 4.5. Location of NEXRADs used for mean bias time series calculation

NEXRAD	Location	Lat	Lon
KFWS	Dallas-Fort Worth, Texas	32.5731	-97.3031
KHGX	Houston, Texas	29.4719	-95.0792
KMLB	Melbourne, Florida	28.1133	-80.6542
KLIX	New Orleans, Louisiana	30.3367	-89.8256

Significant GPM overpasses made with these four radars from April 2014 till October 2017 have been selected. The overpasses are chosen such that sufficient amount of precipitation lies within the Ku swath and 100 Km range circle of the GR. It is very difficult, in each

case, to have overpasses such that precipitation is present common to both inner and outer swath. The reason being since inner swath is narrower, sometimes it does not fall within the 100 Km range of GR. At times, precipitation events may not be wide spread enough to cover the inner swath. This is why, only Ku band has been considered for calculating mean reflectivity bias time series. It is to be noted that the latest version 5 GPM-DPR files have been used in this study. Next volume matching procedure have been performed on every cases and mean reflectivity bias is calculated for each case. The bias calculation has been mathematically defined in equation 16.

4.2.1. MEAN BIAS PLOTS. Mean biases for years 2014 to 2017 for KFWS, KHGX, KMLB and KLIX are presented in figures 4.22, 4.23., 4.24 and 4.25 respectively. It can be seen that for all the radars the mean biases vary between ± 3 dBZ. Radars KFWS and KMLB seem to be well calibrated throughout the years. Radar KHGX exhibits a trend towards positive bias during mid year.

4.3. COMPARISON OF RADAR RAINFALL RATE PRODUCT

In this section, the rainfall rate product from DPR inner swath and outer swath are compared against that of ground radar. The rainfall rate retrieval algorithm of DPR [4] is based on the retrieval of drop size distribution. The parameters that are retrieved are the median drop diameter D_0 and the intercept parameter N_w and a fixed value of mu is considered. In the outer swath where only Ku band data is present, a single frequency rain retrieval process [19] [21] is used. In the inner swath a dual-frequency approach [19] is adopted. Since data at both the frequency are available, two parameters of the drop size distribution can be independently retrieved. These two parameters are D_0 and N_w. Rainfall retrieved in the inner swath is expected to give better estimates than the single frequency
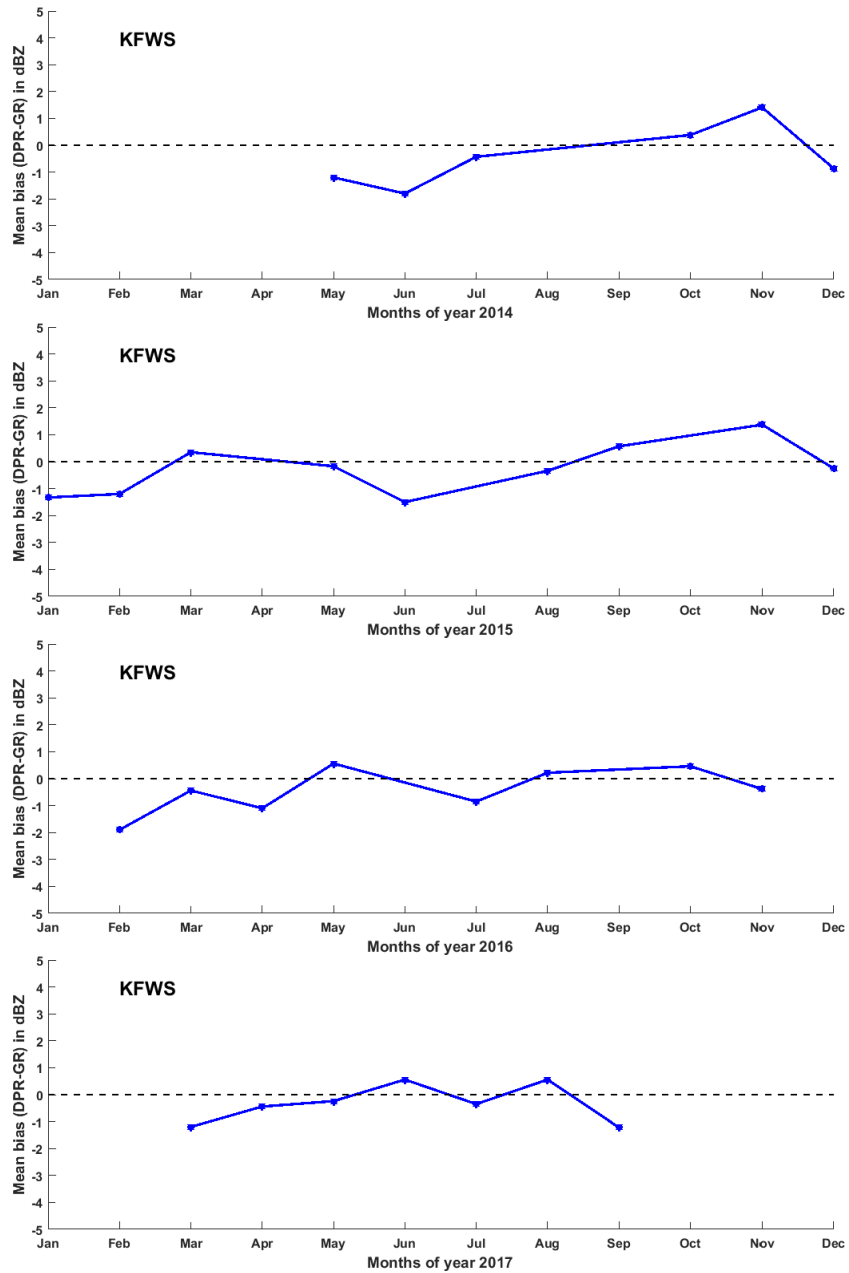
FIGURE 4.22. Time series of DPR-GR mean reflectivity bias for NEXRAD KFWS for years 2014, 2015, 2016 and 2017

retrieval. After the computation of DSD, the rainfall rate is calculated in the Solver Module [19]. In the present version of GPM algorithm, non uniform beam filling effects have also been considered and a procedure for its correction is implemented in the Solver Module [19]. The rainfall retrieval method for dual-polarization ground radar uses a different approach.
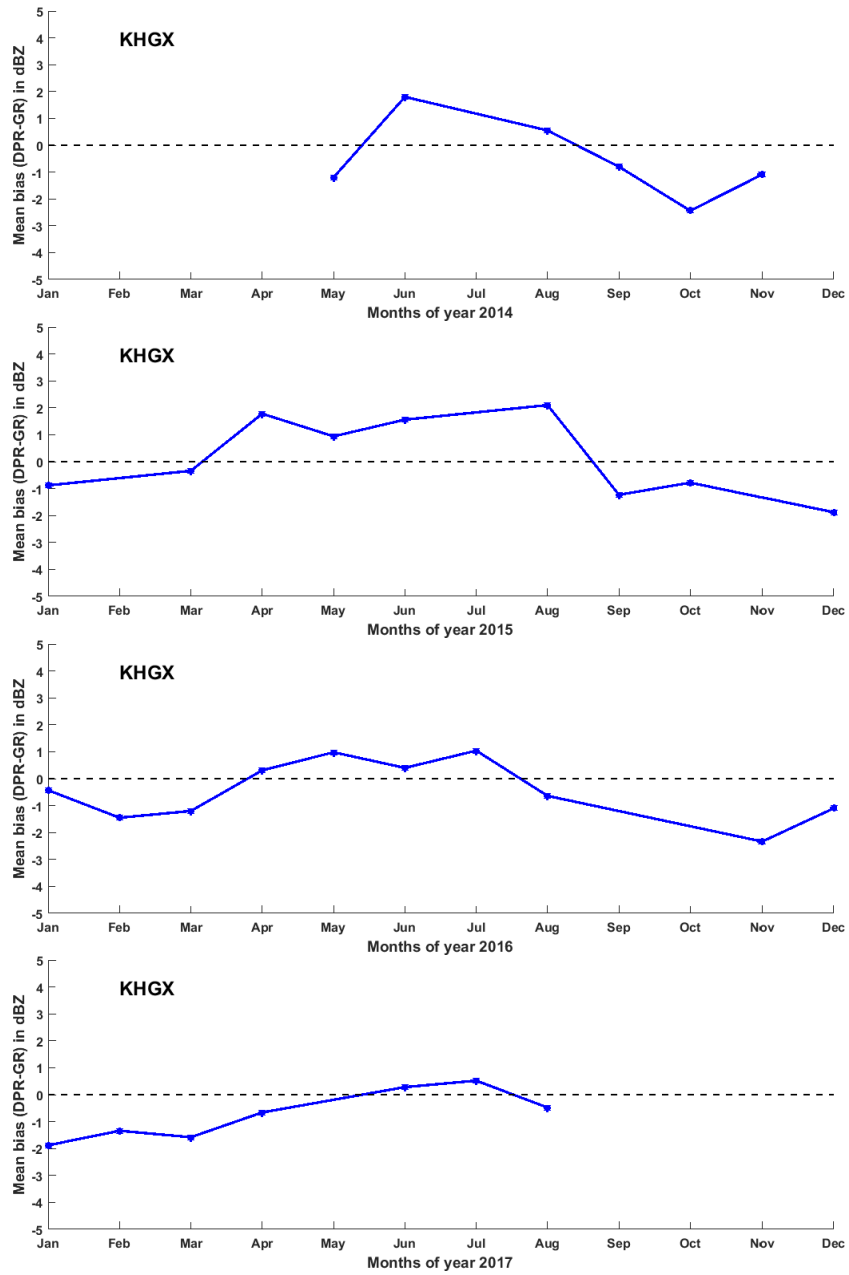
FIGURE 4.23. Time series of DPR-GR mean reflectivity bias for NEXRAD KHGX for years 2014, 2015, 2016 and 2017

The basics remain the same though. Dual-pol moments like Z_{dr} and K_{dp} which are related to the DSD are used along with reflectivity factor to retrieve rainfall. In S-Band, rainfall rate is generally retrieved from a combination Z, Z_{dr} and K_{dp} power law relations. A detail
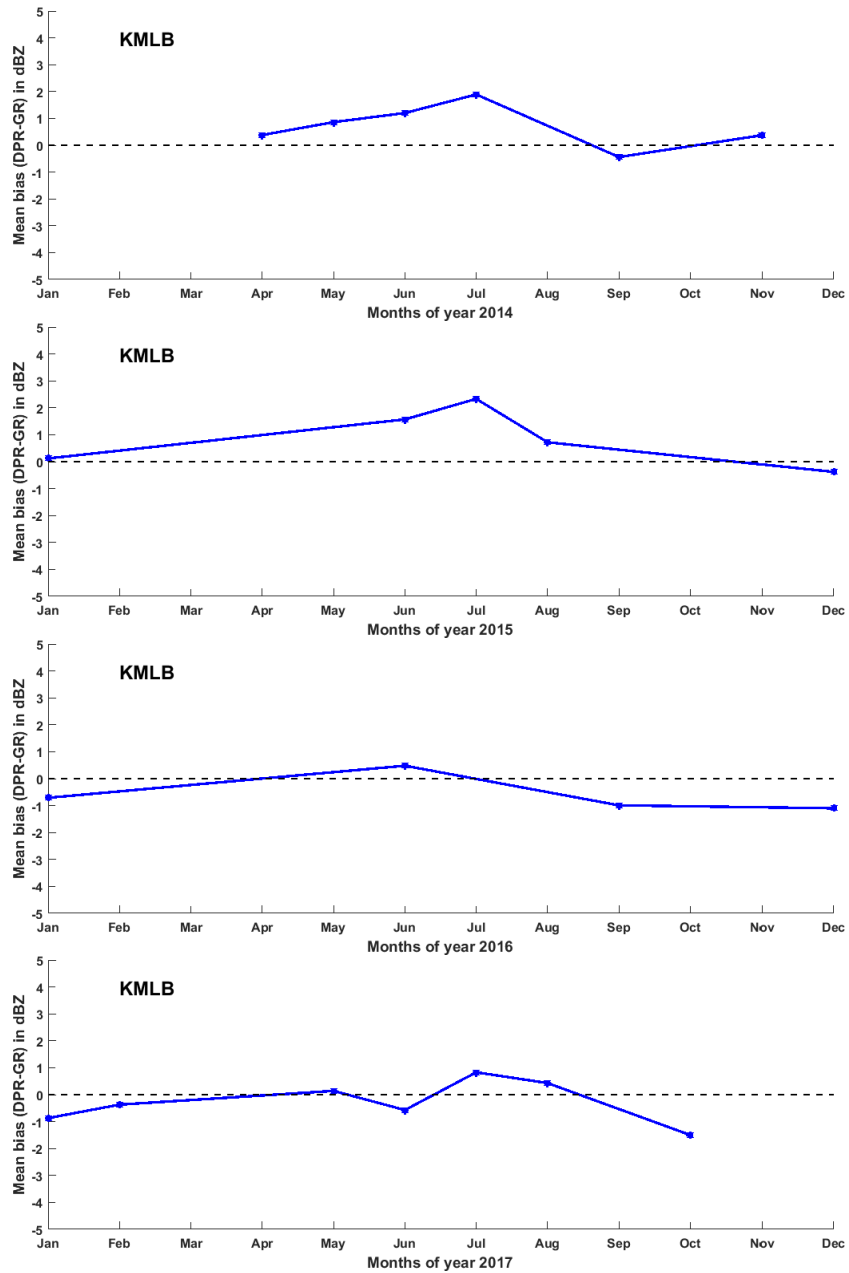
FIGURE 4.24. Time series of DPR-GR mean reflectivity bias for NEXRAD KMLB for years 2014, 2015, 2016 and 2017

description of the methodology for GR rainrate retrieval adopted in this study can be found in [?].

4.3.1. CASE STUDIES. In this study, rainfall rates retrieved from DPR's inner and outer swath is compared with GR's rainfall rate. First, GPM-DPR overpass with GR is collected
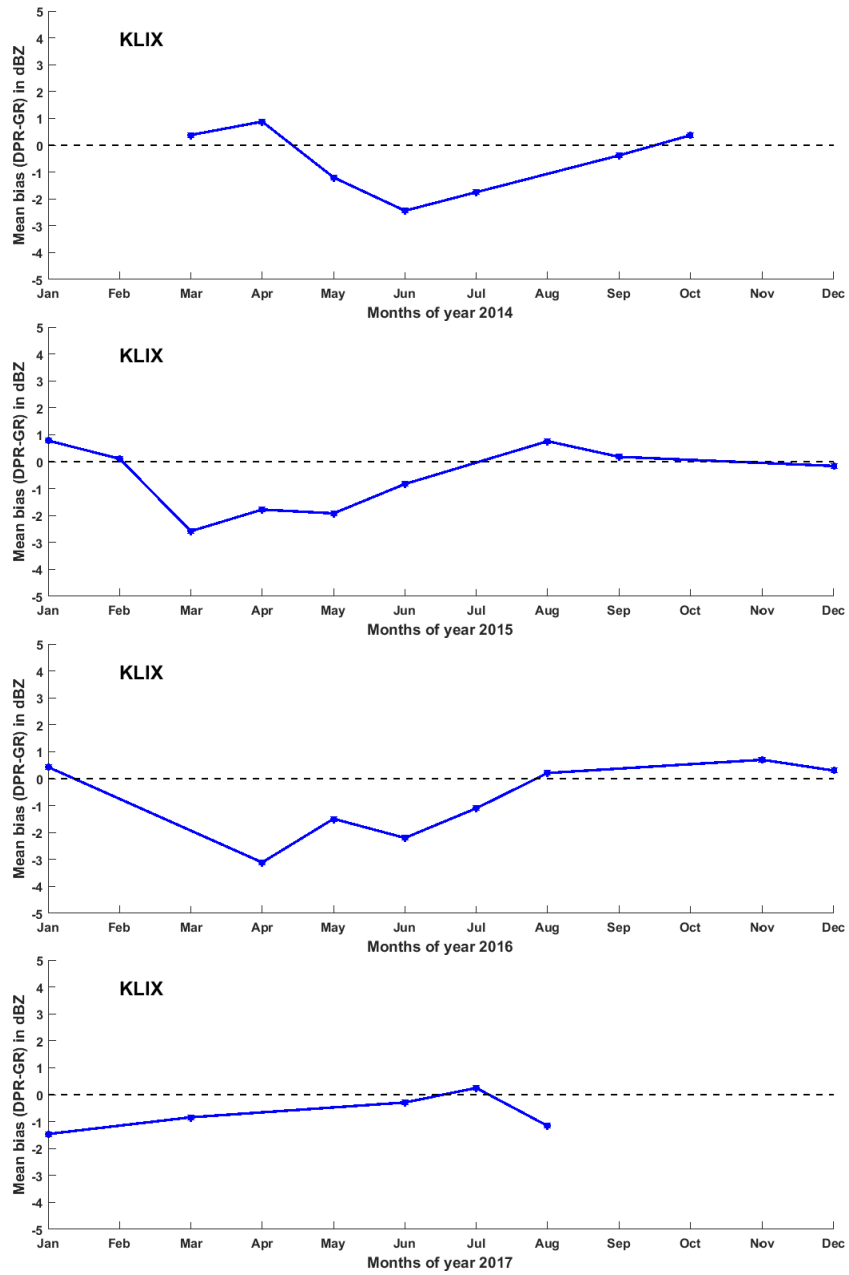
FIGURE 4.25. Time series of DPR-GR mean reflectivity bias for NEXRAD KLIX for years 2014, 2015, 2016 and 2017

and volume matching procedure is conducted. 3 cases which are shown for reflectivity comparison are again considered here.

The first case study is with the NEXRAD KFWS located at Dallas - Fort-Worth in Texas on 3rd March, 2015. The DPR's closest time of approach to the ground radar's location is 08:56:09 UTC. In figure 4.26 volume matched rainfall rate is shown from DPR's outer swath, inner swath and from GR at surface level.
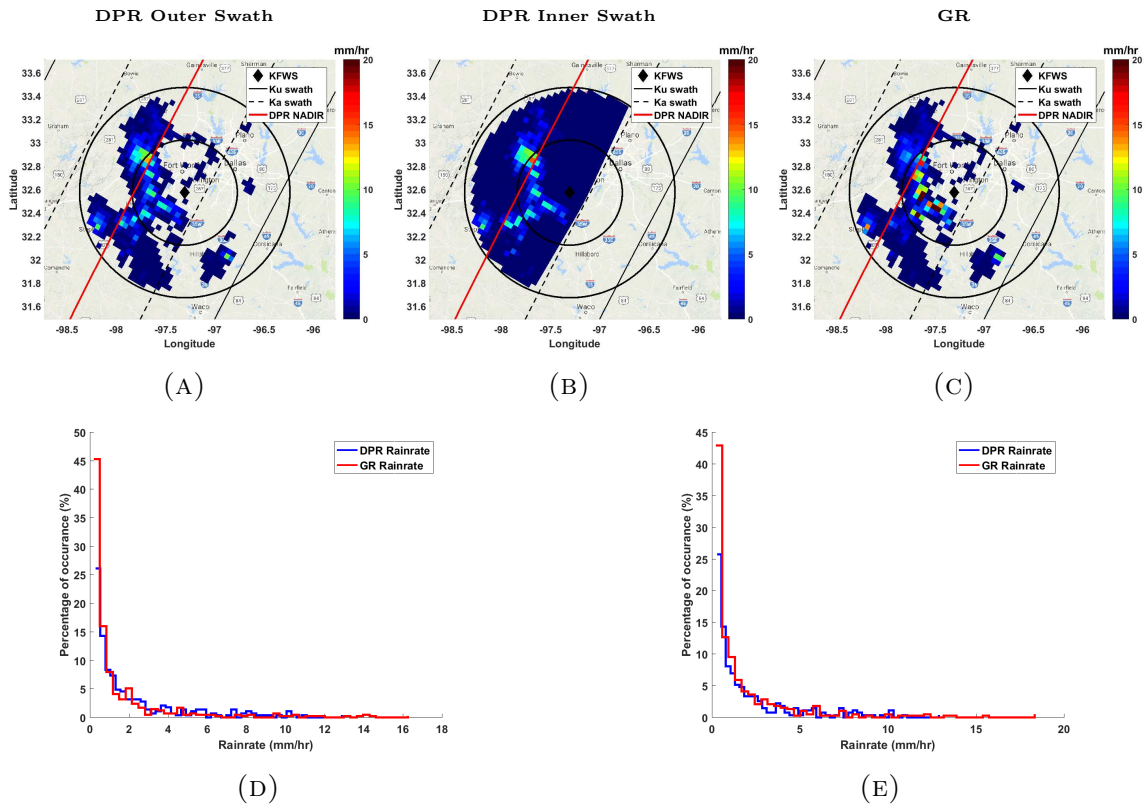
FIGURE 4.26. Volume matched rainfall rate at surface comparison from DPR overpass with NEXRAD KFWS on 3rd March, 2015 at 08:56:09 UTC. (A) DPR Outer swath RR (B) DPR Inner swath rainrate (C) GR rainrate (D) Histogram of DPR outer swath RR vs GR RR (E) Histogram of DPR inner swath RR vs GR RR

The outer black circle corresponds to 100 Km range radius and the inner one corresponds to 50 Km range radius of the GR. The black lines indicate GPM outer swath whereas the dotted lines indicate GPM inner swath. The solid red line is the NADIR. In figure 4.26, the

histograms show the variability of different rainrates. It can be observed that both inner and outer swath are well matched with GR.

The second case is the observations of a mesoscale storm over the New Orleans region from both ground radar KLIX and DPR. The rainfall rates from DPR and GR for this event have been analyzed and made to compare against each other for validation. On 12th August 2016 GPM-DPR made an overpass with NEXRAD KLIX located at New Orleans, Louisiana. The closest time of approach was 12:16:44 UTC.
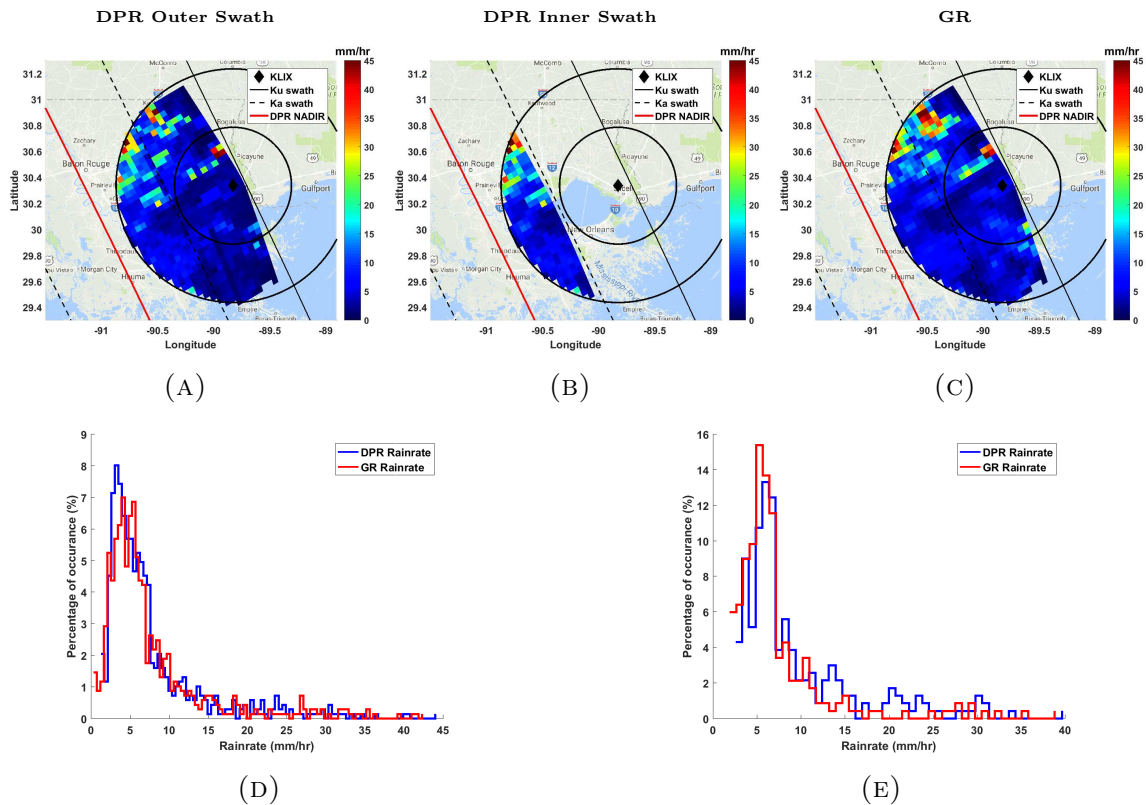
FIGURE 4.27. Volume matched rainfall rate at surface comparison from DPR overpass with NEXRAD KLIX on 12th August, 2016 at 12:16:44 UTC. (A) DPR Outer swath RR (B) DPR Inner swath rainrate (C) GR rainrate (D) Histogram of DPR outer swath RR vs GR RR (E) Histogram of DPR inner swath RR vs GR RR

The outer black circle corresponds to 100 Km range radius and the inner one corresponds to 50 Km range radius of the GR. The black lines indicate GPM outer swath whereas the dotted lines indicate GPM inner swath. The solid red line is the NADIR. In figure 4.27, the histograms show the variability of different rainrates. In this case the number of DPR's pixels showing lower as well as higher rainrate is more than that of GR's.

The third one is the GPM DPR overpass with Hurricane Ana on 19th October 2014, after its landfall at Molokai, Hawaii islands. The ground radar located at this place is NEXRAD PHMO. The closest time of DPR's approach with the GR is 18:48:12 UTC.
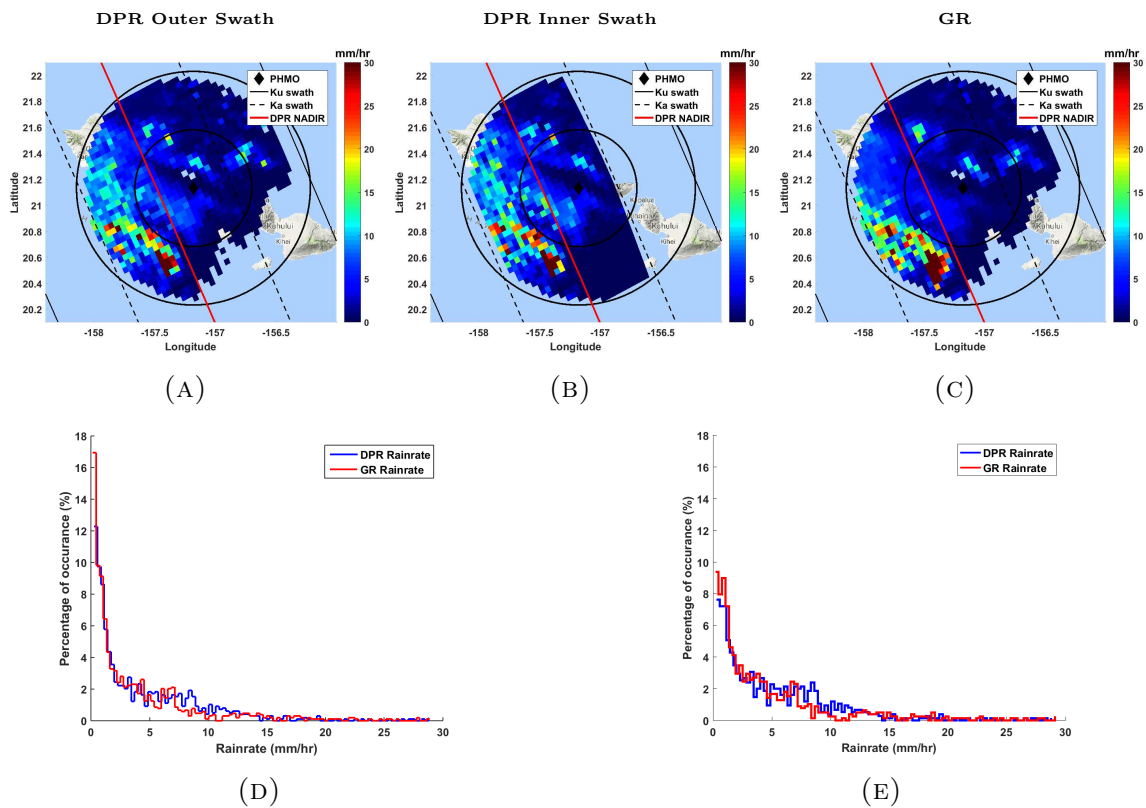
FIGURE 4.28. Volume matched rainfall rate at surface comparison from DPR overpass with NEXRAD PHMO on 19th October 2014 at 18:48:12 UTC. (A) DPR Outer swath RR (B) DPR Inner swath rainrate (C) GR rainrate (D) Histogram of DPR outer swath RR vs GR RR (E) Histogram of DPR inner swath RR vs GR RR

The outer black circle corresponds to 100 Km range radius and the inner one corresponds to 50 Km range radius of the GR. The black lines indicate GPM outer swath whereas the dotted lines indicate GPM inner swath. The solid red line is the NADIR. In figure 4.28, the histograms show the variability of different rainrates. It is observed from the histograms that lower rainfall rates are well matched but higher rainfall rates have more number of samples from DPR as compared to GR.

CHAPTER 5

STUDY OF GPM-DPR PROFILE CLASSIFICATION MODULE

5.1. INTRODUCTION

In this chapter, two of the methods implemented in GPM-DPR profile classification module are considered for validation purposes. They are melting layer detection and surface snowfall detection. These products are cross validated with the dual-polarization measurements from ground radars. An algorithm for hydrometeor classification from ground radar observations [22] has been considered here for comparing the DPR products.

5.2. MELTING LAYER DETECTION BY DFR METHOD VERIFICATION WITH GROUND RADARS

Melting layer detection algorithm has been implemented in the profile classification module. It plays an important role in rain type classification. It is performed on a pixel by pixel basis. It is essential to detect the bright band feature before proceeding with rainfall type classification. Generally rainfall type can be classified into two broad categories, stratiform and convective. The stratiform type is characterized by wide spread occurrence and weak intensity. This type of rainfall exhibits a bright band feature in the back scattered echo which is increase in reflectivity during the melting process. Presence of this feature helps in determining the rainfall type.

The melting layer is the region where the melting process of ice particles starts and ends with conversion in rain drops. In the outer swath where only Ku band data is available the BB detection is made by V-method (vertical profiling method) and H-method (horizontal pattern method) [23]. In the inner swath where both Ku and Ka band data are available, a

dual-frequency ratio method measured or DFR_m developed by Minda et. al. [20] is used to detect melting layer top and bottom heights. This method uses the difference in reflectivity values at the two frequency for detection of the BB. The results from the Ku-only algorithm are combined with that of the DFR_m method of make the BB detection more reliable.

In this study, the melting layer top and bottom information processed for the DPR inner swath is cross verified. Two events observed by the NASA N-POL radar have been selected. Hydrometeor classification [22] is first performed on the GR data to get the different particle types. The region in the GR classification where particle type is wet snow corresponds to the melting layer. Since for volume PPi scans have a coarser vertical resolution , RHI scans from the radar are used for their finer vertical resolution.

(A)

(B)

(C)

(D)
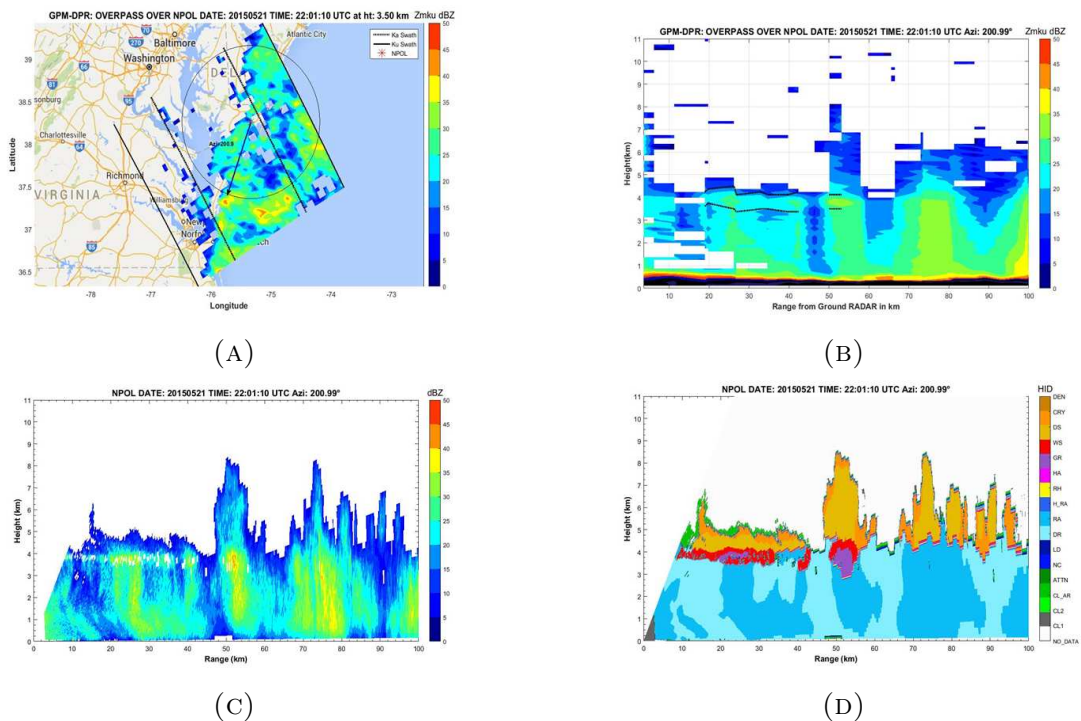
FIGURE 5.1. DPR overpass with NASA N-POL on 18th March, 2015 at 08:56:09 UTC. (A) DPR Ku-band reflectivity (B) DPR Ku-band vertical cut along GR rhi scan (C) GR reflectivity RHI scan (D) GR hydroclass RHI scan

5.3. Identification and validation of snow falling on ground with ground radars

In the current version 5 of GPM DPR Level 2 algorithm, an algorithm for detection of snow falling on ground has been implemented by Minda et. al. [24]. The basic principle of the algorithm is to analyze the DFR_m vertical profile for some typical snow features. The slope of the DFRm profiles is basically controlled by the difference in path integrated attenuation resulting from non-Rayleigh scattering. After analyzing several profiles the authors have found DFR_m snow profiles will have very steep slopes with no BB region. The Ku-band reflectivity for these profiles is generally below 30 dBZ and they also exhibit a low storm top height. A snow profile having these typical features is shown in figure 5.2 from a GPM-DPR overpass on March 17th, 2014 over West Virginia, USA.
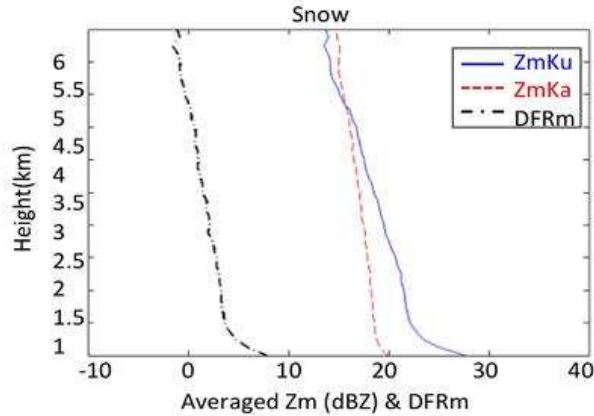
FIGURE 5.2. Vertical profile of reflectivity at Ku and Ka band of snow from GPM overpass with West Virginia, USA on March 17th, 2014.

A parameter called snow index is defined based on the characteristics mentioned above. Mathematically it can be defined as

$$(18) \qquad SI = \frac{mean(|DFRm_{slope}|)}{ZmKu_{max} \times storm\_top\_height}$$

The algorithm implemented into classification module uses this index as a criteria for tagging profiles as snow. Vertical profiles are tagged as snow profiles only if the calculated snow index for that profile is greater than a threshold value. Another important criteria that is checked is the height of the zero degree isotherm. Ideally, it should be within 1Km from the clutter free height. If these two criteria are satisfied then a profile is tagged as snow. A detailed description of the algorithm along with control flowchart can be found in [24].

5.4. Case Studies

4 case studies have been presented here from GPM overpasses with radars such as CSU-CHILL, NASA N-POL and NEXRAD. The data shown for the first two cases are chosen from the OLYMPEx field experiment which took place on the Olympic peninsula of Washington State in USA from November 2015 through February 2016. The S-Band radar on operation during the campaign was NASA N-POL. The first case is a GPM overpass with NASA N-POL radar on 3rd December, 2015 at 15:18:43 UTC. The plots are shown in figure 5.3.

Figures (A) and (C) illustrates reflectivity from N-POL at 0.48^o elevation and DPR Ku-band at 2 Km height. Figure (B) illustrates the results of hydrometeor classification algorithm [22] applied on the ground radar data. It can be observed that both dry and wet snows are present with some crystals occurring over the mountains. Surface snowfall
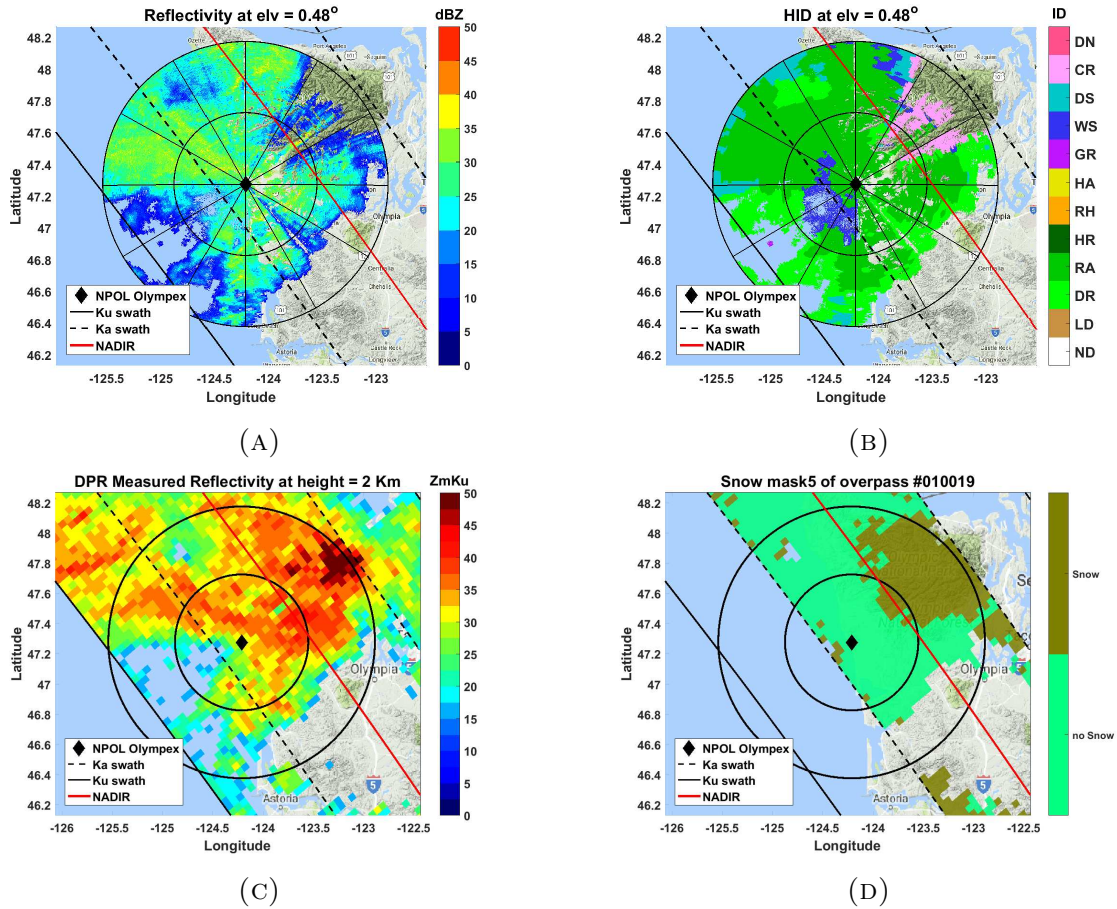
FIGURE 5.3. DPR overpass with NASA N-POL on 3rd December, 2015 at 15:18:43 UTC. (A) GR reflectivity (B) GR hydroclass (C) DPR Ku-band reflectivity(D) DPR snow mask

identification from DPR is shown in figure (D). The location of snow pixels indicated by olive green color matches with that of the ground radar.

Another snow event observed simultaneously by DPR and NASA N-POL radar on 14th November 2015 at 12:56:58 UTC is presented in figure 5.4.

Figures (A) and (C) illustrates reflectivity from N-POL at 1.49^o elevation and DPR Ku-band at 2 Km height. Hydrometeor classification from ground radar data shows dry snow and crystal throughout except a bit of graupel on the inner swath boundary. Snowfall
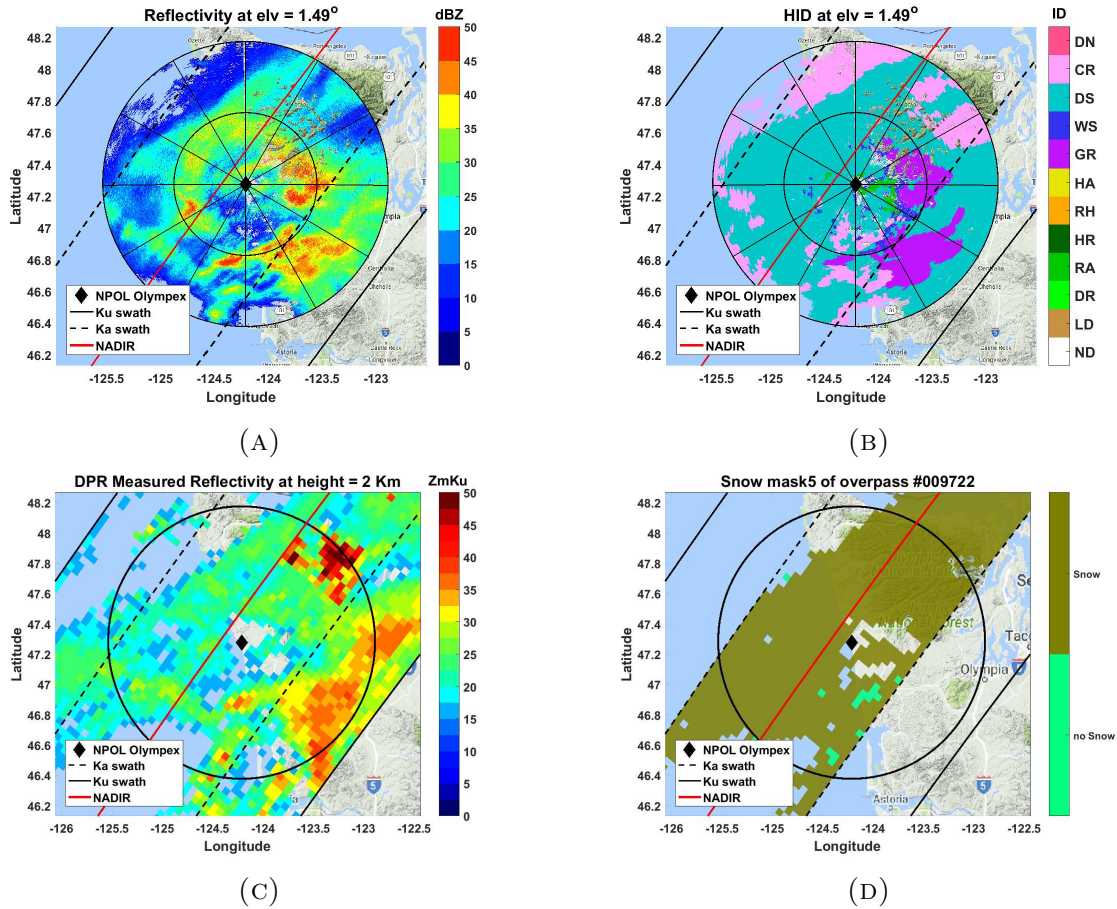
FIGURE 5.4. DPR overpass with NASA N-POL on 14th November 2015 at 12:56:58 UTC. (A) GR reflectivity (B) GR hydroclass (C) DPR Ku-band reflectivity(D) DPR snow mask

identification from DPR also shows snow for most of the scan with few pixels classified as no snow corresponding to a little bit of drizzle region. In the region corresponding to graupel classification Ka band signal is lost due to heavy attenuation. For this reason, the DFRm algorithm is not applicable and as a result no data is shown.

The third case is from a GPM overpass with CSU-CHILL radar located at Greeley, Colorado on 16th April, 2016 at 14:30:54 UTC. The picture 5.5 shows a sector scan of a snow event performed by the GR. The GR hydroclass classified the whole data as fry snow. Similar observation can also be ssen from DPR's snow algorithm.
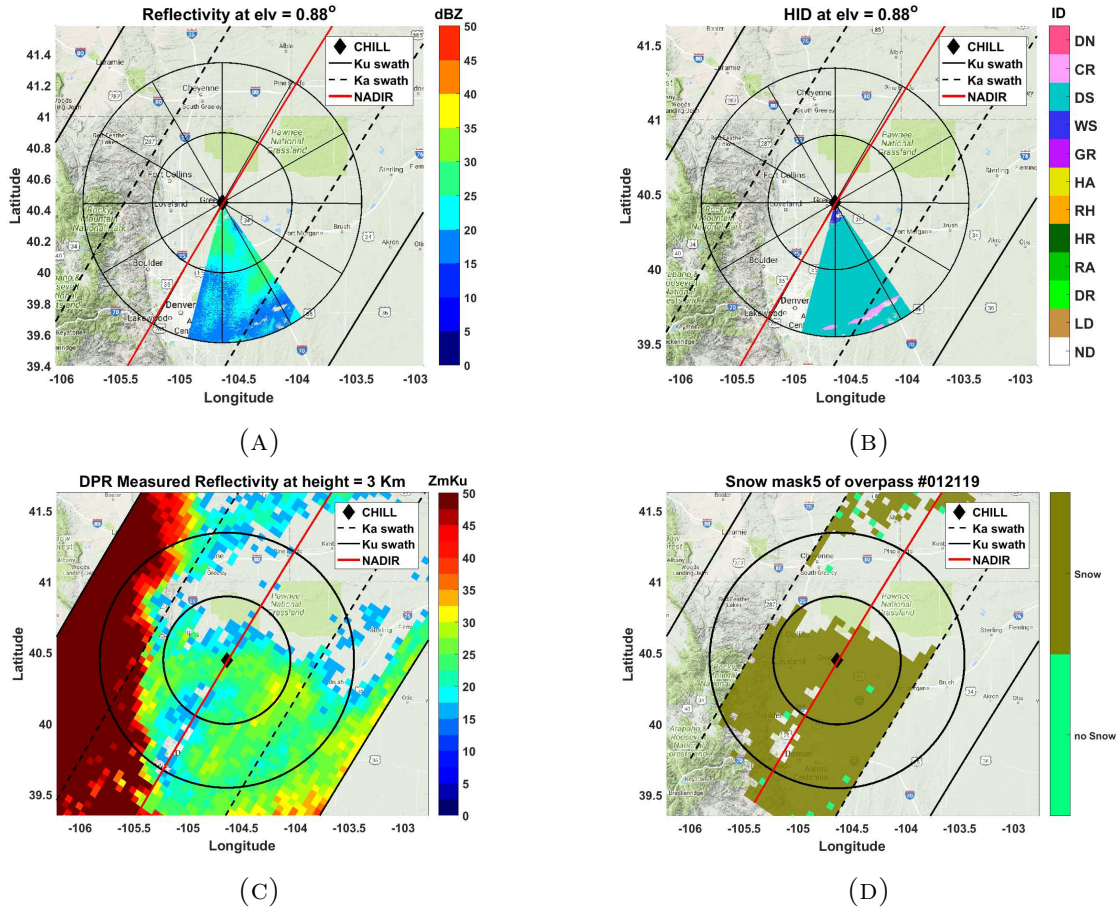
FIGURE 5.5. DPR overpass with CSU-CHILL radar on 16th April, 2016 at 14:30:54 UTC. (A) GR reflectivity (B) GR hydroclass (C) DPR Ku-band reflectivity (D) DPR snow mask

The last case is a snow event observed by both GPM and NEXRAD KIWX located at North Webster, Indiana on 23rd March, 2015 at 15:52:46 UTC. From the figure 5.6, it can be seen that the dry snow region corresponding to the GR is classified as snow from DRR.
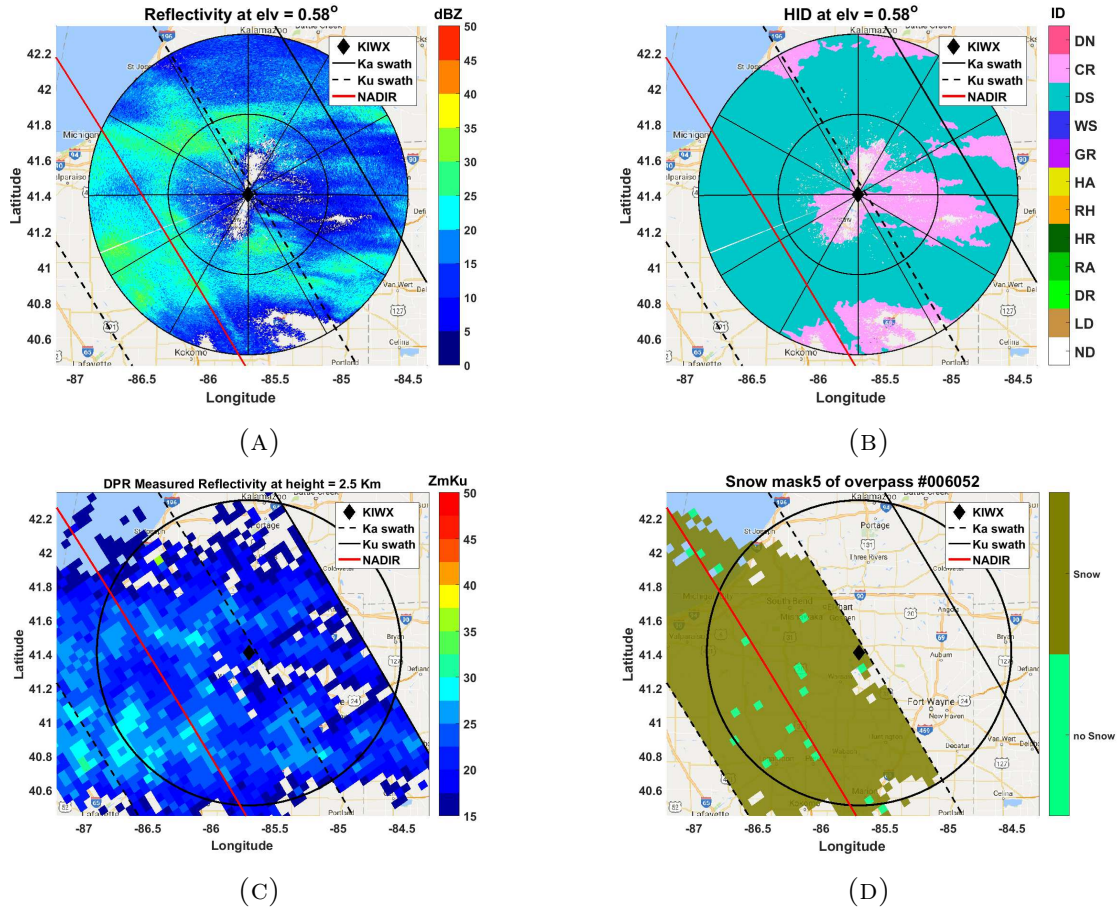
FIGURE 5.6. DPR overpass with NEXRAD KIWX on 23rd March, 2015 at 15:52:46 UTC. (A) GR reflectivity (B) GR hydroclass (C) DPR Ku-band reflectivity (D) DPR snow mask

CHAPTER 6

Summary and Future Work

6.1. Discussions

The primary focus of this research is ground validation of GPM-DPR's measurements and retrievals. Ground validation is important for space radar calibration purposes, and for refinement of retrieval algorithms. Satellite based products such as radar reflectivity, rainfall rate, melting layer height and snowfall identification at ground are cross validated against measurements from ground radar. Single frequency Ku-band only products as well as the dual-frequency Ku and Ka-band based retrieved products both have been used for comparison purposes. An introduction is presented in Chapter 1 whereas Chapter 2 discusses about the GPM satellite and fundamentals of space radar observations and retrieval.

Ground validation is conducted with dual polarization observations from S-band ground radars from various locations, all over the USA. This is presented in Chapter 3. The procedure requires a volume matching technique to be applied on both space radar and ground radar data before proceeding with any kind of comparison. Direct quantitative comparison on a point by point basis is not possible between the space based and ground based system due to difference in viewing angle, operating frequency and resolution volume of both systems. The volume matching methodology takes into account all of these difficulties and also realigns data from both the system on a common grid. DPR's data is only averaged vertically along the beam between the top and bottom gates of the intersection of the GR's sweep. In contrast, the GR data is weighted averaged at the intersection locations within the DPR's footprint which is about 5 Km in diameter. Outcome of this methodology is a set of

vertical profiles located on a same grid. Several case studies are presented that demonstrates this procedure.

In Chapter 4, analysis of some carefully chosen precipitation events simultaneously observed by both GPM-DPR and ground radar have been presented. It should be noted that data points are restricted to those which lies within 100 Km range radius of the ground radar. This is necessary owing to the degradation of ground radar's vertical resolution beyond 100 Km. Beyond 100 Km, for a typical ground radar system, with beamwidth ranging from 0.98^o to 1°, the cross beam resolution is over 1.5 Km. This resolution is not considered sufficient to produce any meaningful comparison. Data are collected such that more than 50 percent of the common overlap region between GPM-DPR and GR has significant amount of precipitation. GPM-DPR's reflectivity and radar rainfall rate are cross validated against that of ground radar's observation in Chapter 4. Data from several ground radars such as NEXRADs, CSU-CHILL and NASA N-POL radar are used in this study. Volume matched reflectivity and rainfall rate are plotted at different horizontal heights and compared against each other. Next, volume matched samples are classified into precipitation type and according to bright band height. Quantitative analysis in terms of scatter plots is presented. Statistical scores such as normalized bias and normalized standard error are used as evaluation metrics. Study of individual storm events revealed that for almost most of the cases the stratiform samples are well correlated as compared to the convective samples. This is due to the heavy attenuation suffered in convective areas of the storms. Samples above the bright band height are found to be well correlated compared to those located below. This can also be explained due to the fact that echoes from region above the bright band received by the space radar are less attenuated. Overall, it has been found that the reflectivity bias

lies within ± 3 dB for almost all the cases which falls within the measurement uncertainty of the space radar. GPM-DPR's rainfall rate based on single and dual-frequency algorithm is also compared with the GR product. Histograms showing variability of both DPR and GR's rainfall rate is presented. GPM-DPR dataset can potentially be used to access the long term calibration of ground radars. Four well calibrated NEXRADs, namely KFWS, KHGX, KLIX and KMLB are chosen for this study. All events occurring at these ground radar location with GPM overpass has been considered within the time period of year 2014 till date. Time series of mean reflectivity bias from these events is calculated for these four radars. The mean bias is found to lie within ± 3 dB. The fluctuation in bias over time can be accounted for variation in type of precipitation from season to season.

In Chapter 5, various products from GPM-DPR's classification module are studied. Melting Layer top and bottom height detection from dual-frequency technique is validated against retrievals from ground radars using dual-polarization algorithms. Research radars, capable of performing RHI scans are used. For case study, stratiform precipitation event having clear bright band signature is considered. Since melting layer height is a dual frequency retrieved product, events observed by GR are carefully selected such there is an overpass with GPM satellite's inner swath. Hydrometeor classification is performed on GR data. Bright band is produced due to melting hydrometeor. For this reason, why wet or melting snow classification is identified from GR data and its height is compared against the melting layer height retrieved using dual-frequency ratio observations. Comparisons show that the heights are well matched. Surface snow fall detection is a new product which has been implemented from version 5 of GPM data. This classification module product is a snow flag which says the presence or absence of snow falling on ground. This feature is also compared and validated

against dual-polarization measurements from GR data. Similar to melting layer detection, the snow flag is calculated from dual frequency observations. A quantity named snow index is used which is calculated using the combination of DFR slope, storm top height and reflectivity at Ku band along with the 0 degree height. Several snow events observed by the ground radar are chosen such that they have overpass with GPM's inner swath. Regions classified as dry snow and ice crystals by hydrometeor classification on ground radar data are compared with the snow flag. After initial study of several snow events, it is found that the satellite product does a good job in classifying vertical profiles as snow. In some cases, very few pixels are wrongly classified. This can be due to very shallow echo regions where storm top height or the zero degree height information is missing. Further study needs to be done for refinement of the algorithm and to make it more robust.

6.2. Suggestion for Future Work

In this work, several events simultaneously observed by both GPM and ground radars are used for validation purposes. It is important to continue routine analysis of overpasses at these radar locations. In addition to the radars used in this study, the ground validation work can be extended to radars located at various parts of the world. It would be quite interesting to study the performance of GPM in observing precipitation occurring at different climatic zones. As a part of extending this research, collaborations are being made with weather and meteorological institutes in Asia. Dual-polarization radars located in Asia could be used to validate GPM-DPR's measurements. In this study, only qualitative comparisons of rainfall rate from GPM-DPR and ground radar are presented. As a future work, rainfall estimates from GPM can be further validated by inter-comparisons with ground based instruments such as rain gauge and disdrometers can be studied.

Bibliography

[1] Y. Senbokuya, S. Satoh, K. Furukawa, M. Kojima, H. Hanado, N. Takahashi, T. Iguchi, and K. Nakamura, "Development of the spaceborne dual frequency precipitation radar for the global precipitation measurement mission," in *International Geoscience and Remote Sensing Symposium*, 2004.

[2] M. R. Schwaller and K. R. Morris, "A ground validation network for the global precipitation measurement mission," *Journal of Atmospheric and Oceanic Technology*, vol. 28, no. 3, pp. 301–319, 2011.

[3] C. Kummerow *et al.*, "The status of the tropical rainfall measuring mission (trmm) after two years in orbit," *Journal of Applied Meteorology*, vol. 39, no. 12, pp. 1965–1982, 2000.

[4] N. Toshio Iguchi, "Possible algorithms for the dual-frequency precipitation radar (dpr) on the gpm core satellite," in *32nd Conference on Radar Meteorology*, 2005.

[5] D. Khajonrat and V. Chandrasekar, "Simulation of spaceborne radar observations of precipitation: Application to gpm-dpr," in *Geoscience and Remote Sensing Symposium, 2008. IGARSS 2008. IEEE International*, vol. 4, pp. IV–455, IEEE, 2008.

[6] V. Chandrasekar and D. Khajonrat, "Simulation of space-borne radar observations of precipitation at ku and ka band," in *Preprints, 34th Conf. on Radar Meteorology, Williamsburg, VA, Amer. Meteor. Soc. P*, vol. 7, 2009.

[7] R. Meneghini, H. Kumagai, J. R. Wang, T. Iguchi, and T. Kozu, "Microphysical retrievals over stratiform rain using measurements from an airborne dual-wavelength radar-radiometer," *Geoscience and Remote Sensing, IEEE Transactions on*, vol. 35, no. 3, pp. 487–506, 1997.

[8] D. Khajonrat, V. Chandrasekar, G. Viswanathan, and V. Shellar, "Simultaneous radar observations of tropical cyclones by space-based and ground-based radar," in *Geoscience and Remote Sensing Symposium, 2007. IGARSS 2007. IEEE International*, pp. 3899–3902, IEEE, 2007.

[9] S. M. Bolen and V. Chandrasekar, "Quantitative cross validation of space-based and ground-based radar observations," *Journal of Applied Meteorology*, vol. 39, no. 12, pp. 2071–2079, 2000.

[10] S. M. Bolen and V. Chandrasekar, "Methodology for aligning and comparing spaceborne radar and ground-based radar observations," *Journal of Atmospheric and Oceanic Technology*, vol. 20, no. 5, pp. 647–659, 2003.

[11] M. Hall, S. Cherry, J. Goddard, and G. Kennedy, "Rain drop sizes and rainfall rate measured by dual-polarization radar," 1980.

[12] J. Simpson, C. Kummerow, W.-K. Tao, and R. F. Adler, "On the tropical rainfall measuring mission (trmm)," *Meteorology and Atmospheric physics*, vol. 60, no. 1-3, pp. 19–36, 1996.

[13] T. Iguchi, R. Oki, S. Eric A, and Y. Furuhama, "2-3 global precipitation measurement program and the development of dual frequency precipitation radar," *Journal of the Communications Research Laboratory*, vol. 49, no. 2, 2002.

[14] J. Awaka, T. Iguchi, H. Kumagai, and K. Okamoto, "Rain type classification algorithm for trmm precipitation radar," in *Geoscience and Remote Sensing, 1997. IGARSS'97. Remote Sensing-A Scientific Vision for Sustainable Development., 1997 IEEE International*, vol. 4, pp. 1633–1635, IEEE, 1997.

[15] D. A. Leone, R. M. Endlich, J. Petrieks, R. T. H. Collis, and J. R. Porter, "Meteorological considerations used in planning the nexrad network," *Bulletin of the American Meteorological Society*, vol. 70, no. 1, pp. 4–13, 1989.

[16] D. B. Wolff, D. A. Marks, E. Amitai, D. S. Silberstein, B. L. Fisher, A. Tokay, J. Wang, and J. L. Pippitt, "Ground validation for the tropical rainfall measuring mission (trmm)," *Journal of Atmospheric and Oceanic Technology*, vol. 22, no. 4, pp. 365–380, 2005.

[17] V. Bringi and V. Chandrasekar, *Polarimetric Doppler Weather Radar*. Cambridge University Press, 1st ed., 2001.

[18] C. W. Ulbrich, "Natural variations in the analytical form of the raindrop size distribution," *Journal of Climate and Applied Meteorology*, vol. 22, no. 10, pp. 1764–1775, 1983.

[19] T. Iguchi, S. Seto, R. Meneghini, N. Yoshida, J. Awaka, M. Le, V. Chandrasekar, and T. Kubota, "Gpm/dpr level-2 algorithm theoretical basis document," 2017.

[20] M. Le and V. Chandrasekar, "Precipitation type classification method for dual-frequency precipitation radar (dpr) onboard the gpm," *Geoscience and Remote Sensing, IEEE Transactions on*, vol. 51, pp. 1784–1790, March 2013.

[21] M. Le and V. Chandrasekar, "Raindrop size distribution retrieval from dual-frequency and dual-polarization radar," *Geoscience and Remote Sensing, IEEE Transactions on*, vol. 50, pp. 1748–1758, May 2012.

[22] R. Bechini and V. Chandrasekar, "A semisupervised robust hydrometeor classification method for dual-polarization radar applications," *Journal of Atmospheric and Oceanic Technology*, vol. 32, no. 1, pp. 22–47, 2015.

[23] J. AWAKA, T. IGUCHI, and K. OKAMOTO, "Trmm pr standard algorithm 2a23 and its performance on bright band detection," *Journal of the Meteorological Society of Japan. Ser. II*, vol. 87A, pp. 31–52, 2009.

[24] M. Le, V. Chandrasekar, and S. Biswas, "An algorithm to identify surface snowfall from gpm dpr observations," *IEEE Transactions on Geoscience and Remote Sensing*, vol. 55, pp. 4059–4071, July 2017.